Photonics with hexagonal boron nitride

Joshua D. Caldwell[1], Igor Aharonovich[2], Guillaume Cassabois[3], James H. Edgar[4], Bernard Gil[3] and D. N. Basov[5]*

Abstract | For more than seven decades, hexagonal boron nitride (hBN) has been employed as an inert, thermally stable engineering ceramic; since 2010, it has also been used as the optimal substrate for graphene in nanoelectronic and optoelectronic devices. Recent research has revealed that hBN exhibits a unique combination of optical properties that enable novel (nano) photonic functionalities. Specifically, hBN is a natural hyperbolic material in the mid-IR range, in which photonic material options are sparse. Furthermore, hBN hosts defects that can be engineered to obtain room-temperature, single-photon emission; exhibits strong second-order nonlinearities with broad implications for practical devices; and is a wide-bandgap semiconductor well suited for deep UV emitters and detectors. Inspired by these promising attributes, research on the properties of hBN and the development of large-area bulk and thin-film growth techniques has dramatically expanded. This Review offers a snapshot of current research exploring the properties underlying the use of hBN for future photonics functionalities and potential applications, and covers some of the remaining obstacles.

[1]*Department of Mechanical Engineering, Vanderbilt University, Nashville, TN, USA.*

[2]*School of Mathematical and Physical Sciences, Faculty of Science, University of Technology Sydney, Ultimo, NSW, Australia.*

[3]*Laboratoire Charles Coulomb, UMR 5221 CNRS-Université de Montpellier, Montpellier, France.*

[4]*Tim Taylor Dept. of Chemical Engineering, Kansas State University, Manhattan, KS, USA.*

[5]*Department of Physics, Columbia University, New York, NY, USA.*

**e-mail: Josh.caldwell@vanderbilt.edu*

https://doi.org/10.1038/s41578-019-0124-1

Since the advent of graphene[1–3], the field of atomically layered quantum materials has expanded exponentially[4]. More recently, heterostructures comprising 2D materials[5] have been realized, and the influence of the transition from 3D to 2D confinement upon the optical, electrical and mechanical properties of 2D materials has been explored. The most widely utilized 2D material in heterostructures is hexagonal boron nitride (hBN), primarily owing to its role as the 'ideal substrate' for graphene[6,7] (FIG. 1) and other atomically layered materials. Bulk crystals of hBN can be exfoliated down to a single atomic plane and exhibit outstanding chemical stability, even in monolayer form. Moreover, hBN is an excellent encapsulant and gate dielectric for heterostructures of transition metal dichalcogenides (TMDs) and other 2D materials[8]. Specifically, encapsulating graphene in hBN protects it from the local environment and dramatically enhances electronic transport, with mobility values surpassed only by those of suspended graphene[6,7,9]. This increase in mobility within hBN/graphene/hBN structures improves the lifetime of surface plasmon polaritons (combined excitations of a free-carrier oscillation and a photon)[9] and also enables their ballistic propagation at cryogenic temperatures[10].

Now, hBN is emerging as an exciting material in its own right, offering novel material properties that enable a broad range of optical[11–13], electro-optical[9,14] and quantum optics[15] functionalities (BOX 1; FIG. 1). Its highly anisotropic crystal structure, properties and polar chemical bonds can be exploited in device applications in IR nanophotonics through the formation of hyperbolic phonon polaritons (BOX 2) in a natural material[11,12]. Its point defects exhibit single-photon emission properties (BOX 3), providing quantum emitters from the visible to the near-IR range, even at room temperature[15]. Moreover, even though hBN is an indirect, wide-bandgap semiconductor (bandgap ~6 eV)[16], it offers very high internal quantum efficiency for deep UV emission. Finally, it exhibits strong, thickness-dependent optical nonlinearities[17,18], and novel optical and electrical properties have been realized within hBN-based moiré heterostructures as a function of the rotation angle between the constituent layers[19–21].

To realize the potential of hBN for device applications, materials synthesis and processing techniques must be advanced, including bulk crystal growth, thin-film deposition, etching, metallization and device integration. Significant advancements in the synthesis of bulk, high-quality, isotopically enriched materials[22,23] improved the prospects for some of these nascent applications. These efforts are in the early stages, but advances in bulk growth[24], chemical vapour deposition (CVD)[25] and molecular beam epitaxy (MBE)[26,27] have been reported. In addition to growth, several other scientific and engineering challenges must be addressed. This Review provides an overview of the state-of-the-art for hBN research

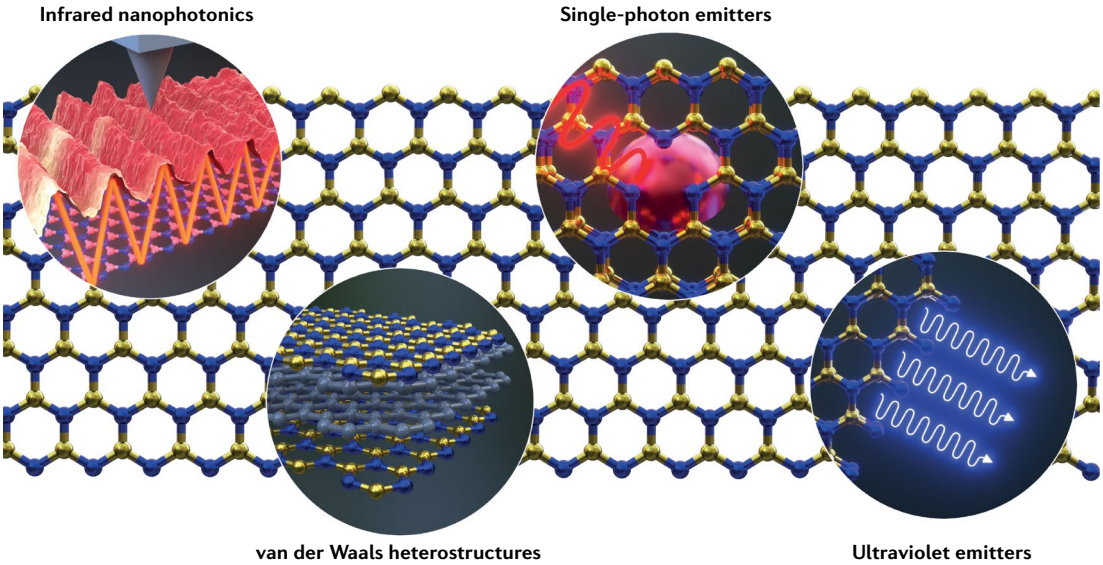

Fig. 1 | **Overview of hBN-based applications.** Hexagonal boron nitride (hBN) was initially identified as an ideal substrate for van der Waals heterostructures, especially for graphene. However, further investigations have demonstrated that this material has exciting properties for nanophotonics in the IR, owing to its ability to support hyperbolic polaritons in its natural state. At the same time, crystallographic defects have been identified as extremely bright single-photon emitters. Finally, despite having an indirect bandgap, hBN offers strong UV emission.

in photonics, including IR nanophotonics, quantum optics, nonlinear optics and UV optoelectronics, and in sample growth and moiré heterostructures.

Infrared nanophotonics

The field of nanophotonics focuses on confining and manipulating light at the nanoscale. In the visible spectral domain, this can be achieved with polaritons supported with noble metals or even using materials featuring a high index of refraction, as the free-space wavelengths are only on the order of a few hundred nanometres. However, in the IR, experimental access to nanoscale confinement is significantly more complicated owing to the long free-space wavelengths[28]. Thus, practical IR nanophotonics demands alternative methods for compressing the free-space wavelengths. This can be achieved through the use of polaritons, quasi-particles comprising a free-space photon and a coherently oscillating charge, which enable the diffraction limit to be surpassed[29,30]. Among 2D materials, a broad range of hybrid light–matter polaritons have been identified, including surface plasmon polaritons and surface phonon polaritons, which are the most prevalent[31,32].

Hyperbolic properties of hBN. That hBN is naturally a hyperbolic material (BOX 2) was one of the most intriguing findings in 2D-material-based IR nanophotonics[11,12,33]. As in nanoelectronic applications, in nanophotonics, hBN was originally used as the ideal substrate for graphene-based plasmonic devices[9,34] owing to its crystal structure, which closely matches that of graphene (~1.8% lattice constant mismatch). Specifically, encapsulating graphene between two slabs of hBN increases the graphene plasmon lifetime by a factor of 5, up to 500 fs (REFS[9,35]). However, after 2014, when the natural hyperbolic behaviour of hBN was demonstrated[11,12] (BOX 1), research into the IR nanophotonic opportunities afforded by hBN itself began in earnest.

In hBN, polaritons can be stimulated by coupling IR photons with the polar lattice of the hBN crystal, forming hybrid modes referred to as phonon polaritons[30]. Because of its highly anisotropic crystal structure, hBN exhibits two separate branches of optic phonons within the phonon dispersion, one arising from the in-plane and one from the out-of-plane lattice vibrations (BOX 1). The transverse optic (TO) phonons are IR active and exhibit extraordinary oscillator strength, which provides prominent absorption resonances. These TO phonons, along with the large crystal anisotropy, result in a highly birefringent IR dielectric function[11,12,22]. Furthermore, the polar nature of the bonds in hBN breaks the degeneracy of the longitudinal optic (LO) and TO phonon frequencies, causing a spectral splitting; the region between these frequencies is commonly referred to as the Reststrahlen band[30,33,36]. It is within this band that the permittivity becomes negative (FIG. 2a) and surface phonon polaritons can be supported.

Specifically, for hBN, there are two Reststrahlen bands (lower Reststrahlen, 12.1–13.2 μm and upper Reststrahlen, 6.2–7.3 μm) and both are hyperbolic[11,12]. Hyperbolicity (BOX 2) is an extreme form of birefringence, with the property that the dielectric function is not merely different along orthogonal crystal axes but is negative along certain crystal directions and positive along others[37]. The presence of both type I and type II hyperbolic response in hBN is intriguing because, for the first time, it provides experimental access to hyperbolic modes of both types within the same material system and geometry. The inversion of the sign of the real part of the dielectric function along the out-of-plane and in-plane directions between these two bands results in the inversion of the sign of the polariton dispersion curves within the two Reststrahlen

Box 1 | **Properties of hBN**

Hexagonal boron nitride (hBN) is a highly anisotropic crystal, consisting of boron and nitrogen atoms strongly bonded in the in-plane direction. Because the difference in electronegativity between boron and nitrogen is larger than 0.4 eV, the B–N bond is polar covalent. Out of plane, there are only van der Waals bonds between adjacent sheets, as is the case with graphite. Although hBN is an indirect bandgap semiconductor (with an energy gap of ~6 eV), it exhibits an exceptionally high internal quantum efficiency for deep UV emission (up to 40%). Owing to the highly anisotropic crystal structure of hBN, the frequencies of the normal lattice vibrational modes (optic phonons) are also highly anisotropic, with two distinct optic phonon branches. These are designated as the upper ($\lambda_{FS} \approx 6.2–7.3$ μm) and lower ($\lambda_{FS} \approx 12.2–13.1$ μm) bands, derived from in-plane and out-of-plane phonons, respectively, where λ_{FS} respresents the wavelength in free space. Owing to the polar nature of the bond, the transverse optic and longitudinal optic phonons of each branch are spectrally separated, forming a highly reflective 'Reststrahlen band'. Within this band, surface phonon polaritons can be supported; with the optic phonons, along with the acoustic phonons, forming phonon sidebands in the UV luminescence spectrum.

The electronic band structure of hBN is shown in the figure below, with the conduction states in red, with a minimum at the M point of the first Brillouin zone, and the valence states in blue, with a maximum around the K point. Therefore, both extrema are located at the edges of the first Brillouin zone. The wavevector connecting the M and K points corresponds to T, which sits in the middle of the Γ–K line. Image of the band structure adapted with permission from REF.[140], APS.

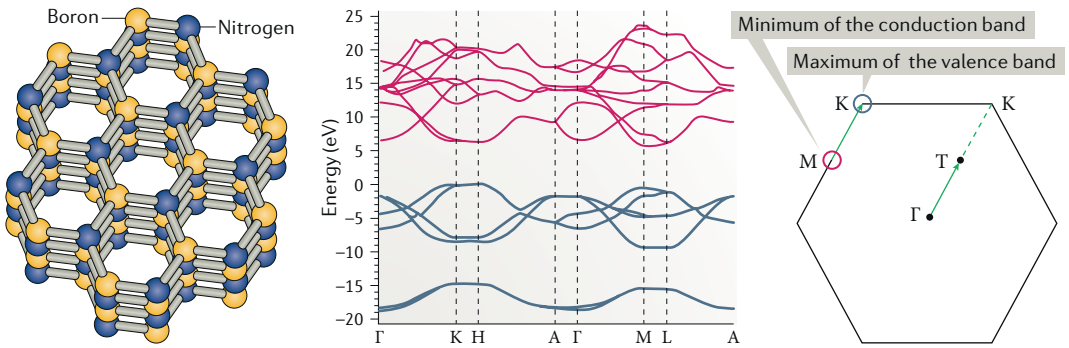

bands (FIG. 2b). Contrary to the initial understanding[12,38], this inversion in the sign of the dispersion results in a negative phase (rather than group) velocity of the hyperbolic phonon polaritons within the type I lower Reststrahlen band[39]. These modes also propagate at exceptionally slow velocities, as slow as $0.002c$ (REF.[39]), where c is the speed of light in vacuum, offering significant promise for applications in enhanced chemical sensing[40]. It is owing to these exotic properties that hyperbolic media have been widely sought after in the context of super-resolution imaging via the hyperlensing concept[41–43], negative refraction[22,44–47], superscattering for enhanced spectroscopy[48] and many quantum nanophotonic concepts[49].

Within an infinite, loss-less slab of a hyperbolic medium, the hyperbolic isofrequency contours support arbitrarily large wavevectors (BOX 2). For real systems, loss is of course unavoidable and it dictates the maximum wavevector attainable. Practically speaking, wavevectors on the order of $k \approx 8 \times 10^5$ cm^{-1} have been reported for higher-order hyperbolic phonon polaritons in monoisotopic hBN[22]. Beyond the influence of loss, the volume confinement of the polaritonic fields induces a thickness dependence in the hyperbolic dispersion[11], resulting in discrete wavevectors supported at a given frequency[37]. The higher-order branches can be identified as the additional blue curves existing at higher momenta (shorter wavelengths) for a given frequency in FIG. 2b.

The hyperbolic modes propagate within the volume of the material, like in a dielectric, but are confined to deeply sub-wavelength dimensions, like in a metal. Although the hyperbolic dispersion dramatically expands the optical density of states by expanding the accessible wavevectors that can be supported at a given frequency, it also results in an added restriction on the polariton propagation, which can only occur at a given frequency-dependent angle. This angle is conserved even following multiple reflections, in violation of Snell's law, as was demonstrated using localized, higher-order hyperbolic phonon polaritons within sub-diffractional hBN cavities[50]. At a given frequency, each of these higher-order modes propagates at the same angle with respect to the surface normal as the fundamental mode. Thus, a superposition of the fundamental and higher-order modes occurs along one trajectory. This was initially visualized[41] as a superposition of the first three orders shown in FIG. 2c (labelled α). The fundamental, second-order and third-order modes of the Fourier components consisting of the waves associated with progressively higher wavevectors (and, thus, shorter polariton wavelengths) are labelled β, γ and ξ, respectively. This approach was later implemented to observe the multiple higher-order modes directly via scattering-type scanning near-field optical microscopy (s-SNOM) for monoisotopic hBN materials, as discussed in REF.[22] (squares in FIG. 2b).

Potential for applications. The hyperbolic properties of hBN offer the promise of a broad range of applications in the mid-IR. For instance, the frequency-dependent polariton propagation provides the basis for hyperlensing[41,51].

Box 2 | **Hyperbolic properties of hBN**

A birefringent material exhibits an anisotropy in the index of refraction along different directions. This results in light propagating through the material at different speeds depending on its polarization axis, a property providing the basis for waveplates. The index of refraction is the square root of the permittivity in the optical spectral range (assuming that the magnetic permeability is 1). A material is hyperbolic if the permittivity is not only different along orthogonal axes but also opposite in sign. This changes the polariton dispersion relationship; this effect is typically illustrated through the use of the isofrequency contours, such as those provided in the figure below. For an isotropic polaritonic material (left), the permittivities are equal and negative, thus, a polariton with a single wavevector (polariton wavelength) per incident frequency can be supported along any direction in space. By contrast, the different signs of the permittivity along different directions in hyperbolic media result in hyperbolic contours (centre and left). A type I hyperbolic material has one axis exhibiting a negative real part of the dielectric function, Re(ε), while a type II material has two. Both forms of hyperbolicity are present within the Reststrahlen bands of hexagonal boron nitride (hBN); type I in the lower band, type II in the upper band. From these hyperbolic isofrequency contours, it can be shown that, at any frequency, any wavevector may be supported, but the propagation is restricted to a defined angle dictated by the surface normal to the isofrequency surface. Because the polariton wavelength is inversely proportional to the wavevector, this means that, in hyperbolic materials, the optical fields can be compressed to arbitrarily small dimensions, with multiple, shorter wavelength modes superimposed in space at any given frequency.

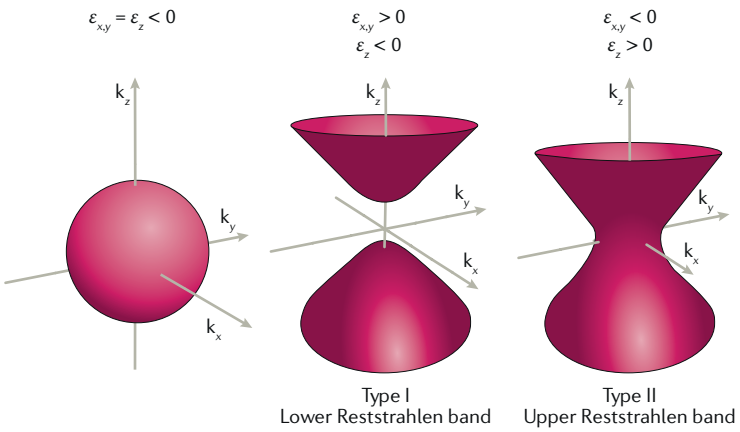

When light is scattered by a deeply sub-wavelength object, evanescent fields are stimulated on the surface of the object. However, these fast-decaying fields cannot be collected by traditional far-field optics. In hyperbolic materials, these scattered evanescent fields can be collected by launching hyperbolic polaritons that propagate through the material and can then be 'read out' on the opposite side by surface probes sensitive to these evanescent fields. These near fields can be probed using tools such as s-SNOM[41,51] (FIG. 3a) or using high-index prisms in the Kretschmann or Otto configurations[52]. However, by expanding the fields to length scales in excess of the free-space wavelength via a curved surface, imaging can be directly carried out in the far field[43]. Unlike visible or UV hyperbolic metamaterial approaches, performing hyperlensing in the mid-IR offers two potential benefits. First, the incident light has low energy and, thus, does not have the risk to excite electronic transitions within the imaged objects or to degrade biological specimens. Second, objects can be imaged in the spectral range in which many materials exhibit strong vibrational absorption signatures. Considering the low losses of polaritons in hBN[22], there is significant potential for label-free bio-imaging with low-energy IR light. Furthermore, the hyperlensing effect can also be used to directly image subsurface features for failure analysis or other quality analysis approaches[53].

Beyond hyperlensing, hBN offers a number of other exciting opportunities for IR nanophotonics. For instance, nanostructures of hBN support a whole range of weak or dark polariton modes, which are optical modes that are forbidden or weakly interacting with incident light, and, through careful design, could be used to dictate the optical angular momentum of the hyperbolic phonon polaritons[54,55]. This, coupled with the multi-branched polariton dispersion, implies an exceptionally large optical density of states. Thus, the hyperbolic properties can be used to modify the emission lifetimes of nearby local emitters or to enhance the IR vibrational absorption of local molecules through the surface-enhanced IR absorption (SEIRA) effect[40] (FIG. 3b). Both applications would significantly benefit from dynamic spectral control.

The volume confinement of hyperbolic materials enables additional opportunities for active tuning of the polariton propagation, beyond what had been previously demonstrated with surface phonon polaritons in quartz coupled with the phase-change material (PCM) $Ge_3Sb_2Te_6$ (REF.[56]). The local ambient environment can be modified through external thermal, optical or electrical stimuli using heterostructures of hBN and PCMs[57] (FIG. 3c). The PCM VO_2 switches between dielectric and metallic phases at relatively low temperatures (~65 °C), which results in dramatic changes in the refractive index[56–58]. When a hyperbolic polariton is launched over the dielectric or metallic domains (blue and red arrows, respectively, in FIG. 3c), it exhibits a different thickness-dependent wavelength (and, thus, wavevector). Additionally, when polaritons are launched in a region over one phase of the PCM and are then transmitted across a domain boundary to a region over the other phase (black arrow in FIG. 3c), the wavelength (wavevector) mismatch induces refraction of the propagating polariton[57]. Thus, by locally controlling the PCM phase, advanced on-chip nanophotonic components can be realized (such as a planar lens or waveguide as outlined in REF.[57]).

Another avenue towards active tuning of phonon polaritons is through free-carrier injection[59,60]. Owing to the large bandgap of hBN, direct carrier injection is not practical. However, the hybridization of hyperbolic phonon polaritons in hBN with surface plasmon polaritons in graphene can lead to their active tuning and modulation through a mechanism similar to carrier injection[14]. The graphene Fermi energy is modified via electrostatic gating, inducing a hybridized surface plasmon polariton–hyperbolic phonon polariton mode with a dispersion extending beyond the upper frequency limit of the Reststrahlen band of hBN (FIG. 3d). This modifies the polariton wavelength or resonant frequency of the hybrid mode and/or modes. This hybrid mode is referred to as an electromagnetic hybrid[61] and holds promise for on-chip nanophotonic metasurfaces and devices, modulators and potentially tunable hyperlensing. Tunable hyperlenses could use the tunable

Box 3 | **Single-photon emitters**

Single-photon emitters (SPEs), sometimes referred to as quantum emitters, are non-classical light sources that emit only one photon per excitation cycle. The detection of single photons is traditionally done using a Hanbury, Brown and Twiss interferometer, in which the incoming photons are split by a 50:50 beam splitter and directed into two avalanche photo diodes (APDs; see the left part of the figure below). A time-correlated, single-photon counting system then detects the arrival times of the photons, generating a histogram of events. If no photons (that is, no coincidence counts) are detected in the same time bin, the system will show a dip, which is evidence of non-classical emission. If the dip at zero delay time is below 0.5, the system can be classified as a single-photon source. Note that normalization to 1 at longer delay times is critically important to provide accurate results.

Defects in solids can be excellent SPEs. They can be described as artificial atoms, with ground and excited states within the host bandgap. Intuitively, the host material should have a large bandgap to accommodate both ground and excited states deep within the bandgap to avoid thermal recombination of carriers (right part of the figure below). These SPEs can be triggered using laser excitation (typically with sub-bandgap energy) or electrical stimuli.

Applications of SPEs include quantum cryptography (also known as quantum communications), quantum sensing and components for quantum computing (such as quantum repeaters or quantum gates). For cryptography, the most important parameter is purity, and the second-order correlation function $g^2(0)$ should ideally be below 10^{-3} to compete with attenuated lasers. Polarized emission and narrow bandwidth (of a few nanometres) would also be advantageous to enable higher signal-to-noise ratios, and hexagonal boron nitride SPEs are excellent contenders. For quantum sensing, the ideal SPE would have access to an optical spin readout, operate at room temperature and be robust. So far, nitrogen vacancy centres in diamond are the most promising SPEs for quantum sensing applications[104]. Finally, for quantum computing, SPEs must be indistinguishable, generated on demand and have gigahertz repetition rate. Applications of SPEs in quantum computing are still in the laboratory phase, with sources based on quantum dots leading the race[188].

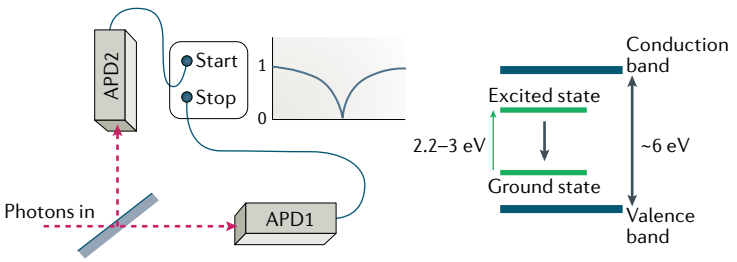

dispersion to modify the hyperbolic isofrequency contour (BOX 2), thereby modifying the propagation angle of the hyperbolic phonon polaritons. This, in turn, would result in a modified expansion of the hyperlens image with respect to the original object[51], without the need for changing the incident frequency, and, therefore, could serve as an alternative method for achieving tunable image magnification.

Unlike hyperbolic metamaterials, in which high ohmic losses in the metallic constituents make many devices impractical, the optic-phonon origin of hyperbolicity in hBN substantially reduces losses[11,12,30] owing to the long scattering lifetimes of optic phonons[30]. These losses can be reduced even further through isotopic enrichment[22], with predicted increases in the optic phonon lifetimes by up to a factor of 14. These long lifetimes have enabled the use of fabrication approaches based on focused ion beam[62] and reactive ion etching[12] to fabricate samples that retained high-quality-factor polaritons (the quality factor Q quantifies the ratio of the stored energy to the rate at which it is dissipated within a cavity). Thus, localized hyperbolic phonon polariton resonators fabricated from hBN exhibit near-record quality factors for sub-diffractional cavities. For sub-diffractional surface plasmon polariton cavities, quality factors on the order of 10 are typical; however, values up to 289 have been reported for hBN nanostructures[12]. Because an increase in the Q factor results in a reduction of the resonance linewidth ($Q = \omega_{res}/\Delta\omega_{res}$, where ω_{res} and $\Delta\omega_{res}$ are the resonant frequency and linewidth, respectively), such high Q values imply the potential for narrow-band thermal emitters[63] and for higher spectral selectivity in matching the hyperbolic phonon polariton resonance to a molecular vibration within SEIRA approaches[40,64]. The former approach was used to create an in-plane hyperbolicity for controlling the polariton wavefront in a planar format[62], a phenomenon that was recently observed in the natural van der Waals crystal MoO_3 (REFS[65–67]). Thus, hBN will continue to serve as a key material for expanding our understanding of hyperbolic polariton physics, while also offering exciting opportunities for realizing next-generation IR optics and active photonic components.

Quantum photonics

Defects in hBN are known to reduce phonon lifetimes, and, thus, are detrimental to its use for IR nanophotonics, but such defects are at the heart of hBN's promise as a single-photon emitter (SPE; BOX 3). Research into quantum photonics with hBN started in 2016, when SPEs in this material were first reported[68]. These SPEs (FIG. 4a) possess high quantum efficiency and brightness (typically over 1×10^6 counts/s), are linearly polarized and, in most cases, are optically stable[69–72]. This set of properties is attractive for practical applications; thus, research into hBN quantum emitters has been rapidly expanding. The origin of the defects from which this emission is derived (their exact crystallographic structure and charge state) is still under debate[73,74], but SPEs are present in a broad variety of hBN types of samples, spanning single crystals[75,76], commercial powders, nanotubes[77] and nano-onions, as well as epitaxial films[78–81] and exfoliated flakes[71]. The emitters can also be engineered in hBN by ion[82] or electron irradiation[83], strain[84], plasma processing[85] or thermal annealing. So far, there is no conclusive protocol to produce emitters operating at a particular wavelength in a deterministic location. This is currently a significant focus within the hBN SPE community. Interestingly, the majority of the emission lines from hBN grown by MBE[78,79] and CVD[80] appear at wavelengths around 600 nm. However, SPEs in exfoliated or commercial hBN materials are distributed over a much broader spectral range, extending approximately from 500 nm to 850 nm.

hBN SPEs are normally excited using a below-bandgap laser, typically emitting blue or green light[86]. However, nonlinear excitation using a short-pulsed laser (on the order of 1 ps) in the near-IR may also be used[87]. Alternatively, anti-Stokes excitation (or photoluminescence upconversion) has been employed for such studies by optically pumping the phonon sideband, which is located approximately 160 meV away from the zero-phonon line[88]. For higher-energy excitations,

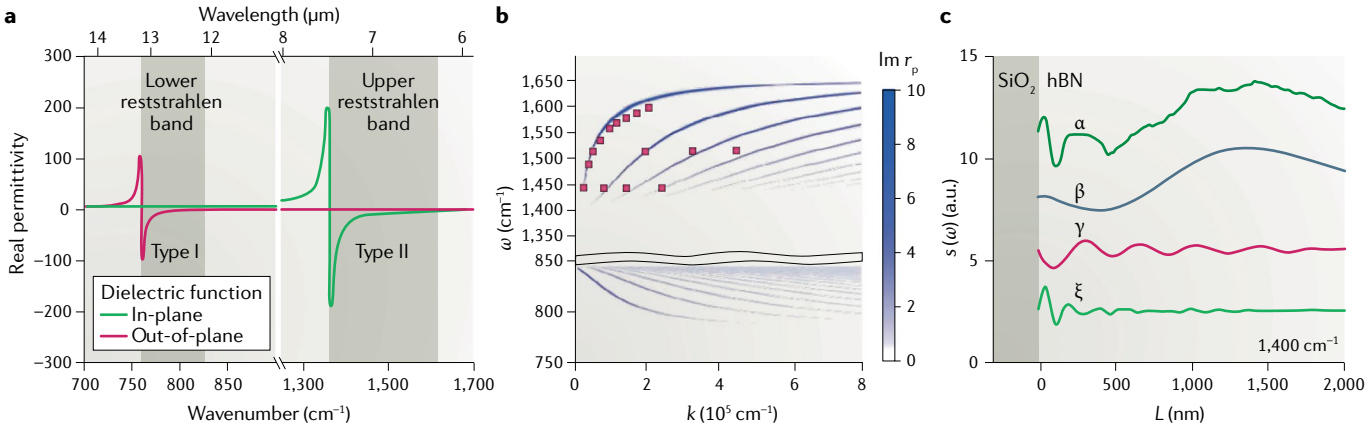

Fig. 2 | **Natural hyperbolic properties of hBN in the mid-IR. a** | The in-plane (ordinary, green) and out-of-plane (extraordinary, red) IR dielectric function of hexagonal boron nitride (hBN). In each of the two Reststrahlen bands, the real part of the permittivity is negative for one of the two directions (ordinary or extraordinary) and positive for the other; thus, hBN is a natural hyperbolic material. **b** | This hyperbolicity results in a multi-branched, thickness-dependent polariton dispersion within each Reststrahlen band (shown here for a 120-nm-thick slab of 98.7% ^{10}B-isotopically enriched hBN), each featuring a progressively larger wavevector (thus, a smaller polariton wavelength) at the same incident frequency. The open white line near 850 cm^{-1} designates the spectral break between the two bands. The inversion in the polaritonic dispersion relations results from the corresponding inversions in the crystal axes featuring negative permittivity, and, thus, in the sign of the phase velocity between the spectral bands[39]. Data points are experimentally derived values from scanning near-field optical microscopy measurements; the lines are the calculated dispersion. r_p is the reflectivity. **c** | The hyperbolicity restricts the polariton propagation to a given frequency-dependent angle confined within the hBN slab, with each of the higher-order modes superimposed along this trajectory. The higher-order modes occur at frequency–wavevector combinations for which integer multiples of the polariton wavelength can be supported along that trajectory, as seen from the line trace obtained from a near-field image measured on an hBN slab close to the interface with a SiO_2 layer (α). The variations in the scattering amplitude s are due to the standing waves created by the interference between the polaritons launched by the tip and those reflected from the slab edge. This superposition (α) may be broken into the Fourier components featuring the fundamental (β), second-order (γ) and third-order (ξ) modes. (a.u., arbitrary units). Panel **a** is adapted from REF.[12], Springer Nature Limited. Panel **b** is adapted from REF.[22], Springer Nature Limited. Panel **c** is adapted from REF.[41], CC-BY-4.0.

cathodoluminescence studies of hBN SPEs can be performed, and SPEs in the UV range have been identified[89]. To date, hBN remains the only platform that can yield SPEs in the deep-UV (~4 eV) range.

For most applications for which SPEs are of interest, narrow emission lines are desirable. They can be achieved at cryogenic temperatures, at which the hBN SPEs exhibit emission linewidths approaching the Fourier transform limit. However, these modes do suffer from severe spectral diffusion (random fluctuations in the emission frequency), which likely originates from the permanent dipole moment of the emitting defect[90–93]. This can be observed in spectra from an SPE in hBN recorded at room and cryogenic temperatures (FIG. 4b). Rigorous density functional theory modelling is currently underway to help understand the energy level structure of the hBN defect states and, thus, to gain the insights necessary to potentially eliminate spectral diffusion[73,74]. Stark shifts[94,95] or strain tuning[96,97] may be employed to stabilize the emission lines; Stark tuning of an SPE in hBN was realized (FIG. 4c). The device contained hBN encapsulated between two graphene layers, which were used to create a strong electric field across the hBN layer[94].

Given the stability and brightness of hBN SPEs and the atomically layered form of the host material, it is appealing to integrate hBN SPEs with photonic and plasmonic nanostructures. For plasmonic devices that employ 2D materials, the most obvious approach is to drop-cast the 2D flake onto metallic pillars. Indeed, this strategy to combine quantum emitters with a plasmonic lattice was realized successfully by fabricating hBN-based hybrid structures in which the SPE is collocated with the high concentrations of the plasmonic optical fields. A modest Purcell enhancement (an enhancement of the spontaneous emission) was measured, resulting in a bright emission exceeding 1×10^6 counts/s (REF.[98]). To realize direct coupling of a surface plasmon polariton to the SPE, the manipulation of individual gold resonators (nanospheres) was attempted using an atomic force microscope (AFM)[99]. In both cases, the SPE was characterized before and after coupling with the surface plasmon polariton, enabling direct comparison to the emission amplitude in the absence of plasmonic enhancement. Thus, such coupled plasmon–SPE approaches offer an interesting platform for studying fundamental physics, as well as for characterizing the overall emission enhancement and resulting optical losses.

Progress has also been made toward integrating hBN SPEs with dielectric optical cavities and waveguides. Initially, a pick-and-place approach for integrating the hBN flakes into optical waveguides was used[100]. However, hBN has the unique property that its structures can be fabricated directly within the host material. Unlike other 2D materials, hBN maintains its optical bandgap even when its thickness is varied from bulk to monolayer.

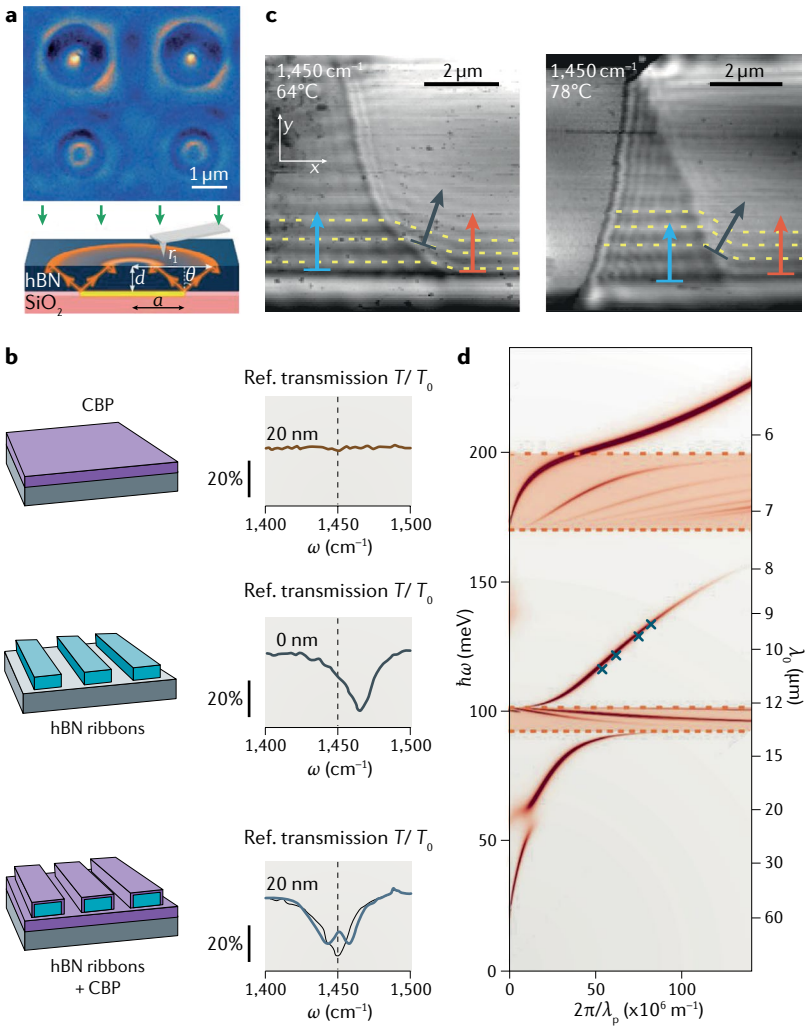

Fig. 3 | **Applications of hyperbolic polaritons within hBN. a** | The frequency-dependent hyperbolic polariton propagation serves as the basis for a broad variety of potential applications, such as hyperlensing[37,45], shown here for successively smaller gold disks underneath a 110-nm-thick hexagonal boron nitride (hBN) slab. The hyperlens concept is demonstrated in the inset schematic: the gold disks act as both antennas and polariton launchers; under IR illumination (green arrows), they launch polaritons from the disk edges that propagate with sub-diffractional focusing towards the hBN top surface, where near-field images are recorded. **b** | A dramatic improvement in IR absorption of a molecular analyte (a 20-nm-thick molecular layer of the organic semiconductor 4,4′-bis(*N*-carbazolyl)-1,1′-biphenyl, CBP) is achieved through the concentrated electromagnetic fields generated by hyperbolic polaritons in hBN nanoribbons (bottom blue curve); the absorption of a bare CBP film is shown for comparison (top brown curve). The spectrum of bare nanoribbons is shown in the middle grey curve. **c** | Active control of hyperbolic polariton propagation can be achieved through heterostructures of hBN with phase-change materials, such as VO_2. Polaritons propagating in the hBN over the metallic (bright domains) and dielectric (dark domains) phases of the phase-change materials exhibit different polariton wavelengths (blue and red arrows), and modes launched from one domain into the other are refracted (black arrows) according to Snell's law. **d** | Another means for active tuning is via hybridization of surface plasmon polaritons in graphene with hyperbolic polaritons in hBN, achieved through electrostatic gating of graphene/hBN heterostructures. This hybridization results in electrical control of the hyperbolic polariton dispersion; the hybrid branches of the dispersion result in a single plasmon–phonon polariton mode extending beyond the upper frequency edge of the hBN Reststrahlen band (shaded regions), in which propagating phonon polaritons normally exist. λ_0, wavelength of the laser source in free-space; λ_p, plasmon wavelength; $\hbar$, reduced Planck's constant; ω, frequency. Panel **a** is adapted from REF.[41], CC-BY-4.0. Panel **b** is adapted from REF.[40], CC-BY-4.0. Panel **c** is adapted from REF.[57], CC-BY-4.0. Panel **d** is adapted from REF.[9], Springer Nature Limited.

Consequently, photonic crystal cavities[101], micro-ring resonators[102] and, more recently, flat lenses[103] have been realized from monolithic hBN. An example of a 1D photonic crystal cavity fabricated from hBN is provided in FIG. 4d. This novel approach has the potential to control light–matter interactions (such as the Purcell enhancement) and realize scalable nanophotonic circuitry within the same material system. However, hBN has one major disadvantage in this regard: its low refractive index in the visible range ($n \approx 1.8$) makes it difficult to confine light exclusively within the hBN structure.

In terms of applications, SPEs in hBN may offer a unique advantage as they are hosted in atomically thin layers that are bio-compatible, inert and can be monolithically integrated within complementary metal–oxide–semiconductor (CMOS)-compatible architectures. However, for sensing purposes, it is necessary to identify electron-spin-dependent transitions associated with the SPE defect states, analogous to the nitrogen vacancy centre in diamond[104]. Progress in this direction has already been initiated, with electron paramagnetic resonance studies of defect ensembles[105] and numerous reports showing magnetic-field-dependent optical transitions[106]. However, there are still no conclusive reports of optically detected magnetic resonance associated with the SPE defect states. An additional application for hBN SPEs is super-resolution imaging. Two independent works have demonstrated that these SPEs can be used in both localization microscopy (down to ~10-nm resolution)[107,108] or ground-state depletion imaging (~70-nm resolution)[109]. Thus, these experiments pave the way for employing hBN SPEs in quantum imaging and quantum sensing of liquid and biological samples.

The initial building blocks for an integrated quantum photonic platform based on hBN SPEs are in place. One of the key remaining challenges is the availability of large-area single crystals and films, which are imperative for practical structures. Likewise, it is necessary to identify the methods by which the spatial and spectral properties of the hBN SPEs may be engineered. Despite these unresolved issues, new opportunities for quantum photonics with hybrid 2D systems are already emerging; based on a recent report[110], hybrid systems involving TMDs integrated into hBN cavities can be realized.

Nonlinear optics. In the previous section, we briefly discussed the nonlinear excitation of the SPEs in hBN, but, speaking more generally, nonlinear interactions — specifically, second-harmonic generation (SHG) — have also been employed to study the crystalline and optical properties of hBN directly. In the case of bulk hBN, the crystal belongs to the centrosymmetric D_{6h} (REF.[4]) space group. However, as the crystal thickness approaches atomic thickness, the symmetry is reduced. For exfoliated flakes, hBN typically has the AA' stacking order; however, another sequence (AB) is also energetically stable[17] (FIG. 5a). The AA' stacking exhibits inversion symmetry, whereas the AB stacking does not. Second-order nonlinearities including SHG vanish in materials exhibiting inversion symmetry. Thus, consistent with this general expectation, a significant SHG response has only been observed in hBN bilayers with AB stacking (FIG. 5b).

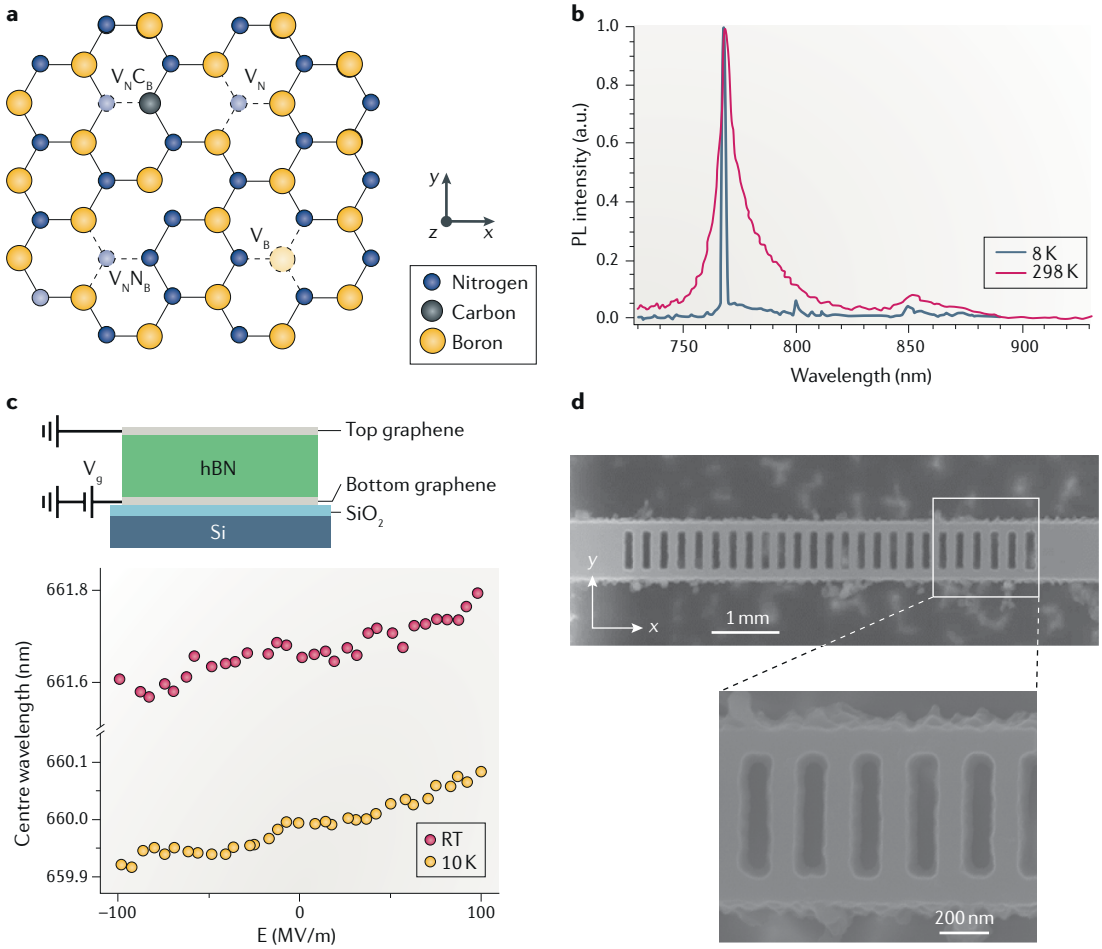

Fig. 4 | **Room-temperature, single-photon emission in hBN. a** | Schematic illustration of potential hexagonal boron nitride (hBN) defects (V_N, nitrogen vacancy; V_B, boron vacancy; V_NC_B, antisite carbon vacancy; V_NN_B, antisite nitrogen vacancy). **b** | Typical photoluminescence (PL) spectra of a single-photon emitter in hBN at room temperature (RT, red) and at cryogenic temperature (blue). The emission is predominantly concentrated at the zero phonon line, which is advantageous for many applications. **c** | Schematic of the device used for Stark-shift tuning of single-photon emitters in hBN. Graphene flakes serve as bottom and top electrodes. A Stark shift is observed at cryogenic and room temperatures. **d** | 1D photonic nanobeam cavity made from an hBN stack exhibiting high quality factors. a.u., arbitrary units. Panel **a** is adapted with permission from REF.[73], ACS. Panel **b** is adapted with permission from REF.[91], ACS. Panel **c** is adapted from REF.[94], CC-BY-4.0. Panel **d** is adapted with permission from REF.[101], ACS.

The SHG signal increases approximately by a factor of 4 in AB bilayer hBN in comparison to monolayer domains, and AA' bilayers have the weakest response (FIG. 5c). Earlier work[18] demonstrated that, in exfoliated hBN, the SHG response was nominally constant for flakes with an odd number of layers (including monolayers), implying that it is the lack of inversion symmetry within the AB stacking that causes the strong SHG response[17]. The relatively constant SHG amplitude for an odd number of layers is due to the fact that the responses from the layers underneath the topmost layer cancel each other owing to inversion symmetry. Thus, only the top monolayer of the hBN flake contributes to the SHG emission within this stacking order. Furthermore, for hBN flakes with an even number of layers, negligible SHG was observed, as expected based on the inversion symmetry[18].

Intriguingly, the SHG amplitude also tracks the crystallographic symmetry. Polarization-dependent SHG data reveal six-lobed patterns when assembled in polar plots. The maximum enhancement of the SHG amplitude was observed when the polarization was aligned with the crystallographic axes of the hBN. Thus, the crystallographic orientation of the hBN microcrystal could be determined from the polarized SHG amplitude, even in the absence of a clear crystal facet[17,18]. Notably, the surface nonlinear susceptibility of hBN monolayers is approximately $d_{hBN}^{s} = 3.0 \times 10^{-32}$ m·C/V², which is comparable to that of other transparent, strongly nonlinear crystals, such as $LiNbO_3$ and β-BaB_2O_4.

A very different class of nonlinear phenomena in hBN has been predicted[98] and is rooted in the hyperbolic phonon polaritons that hBN supports. Provided a two-photon emitter is placed in close proximity to the hBN (<10 nm), the nonlinear emission rate is predicted to drastically exceed that of linear, single-photon emission[111]. The emitter must be located within the evanescent tail of the polaritonic near fields, overcoming the impedance mismatch between free-space light and

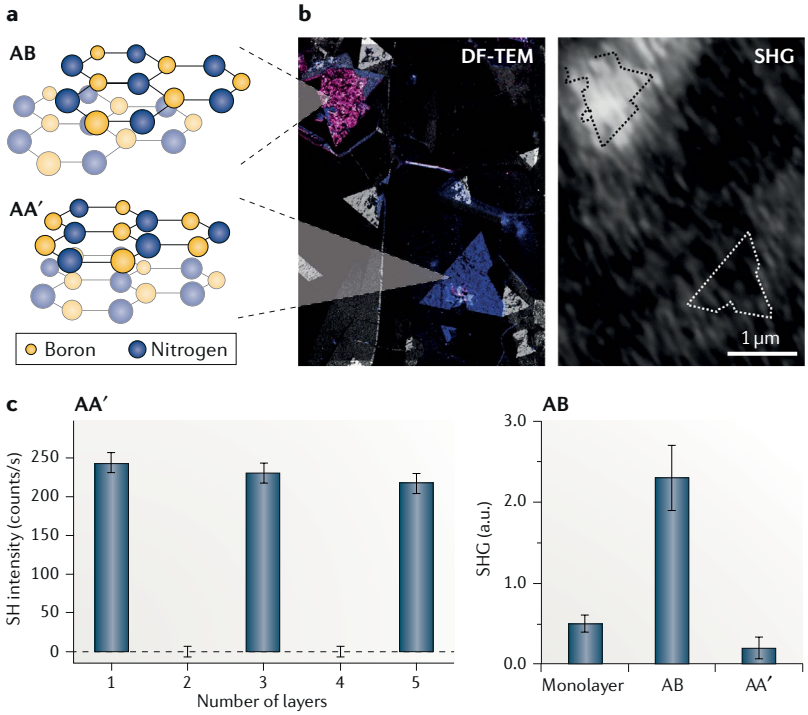

Fig. 5 | **Dependence of second-harmonic generation upon hBN stacking and thickness. a** | The two energetically stable stacking orders for hexagonal boron nitride (hBN). **b** | Dark-field transmission electron microscope (DF-TEM) images of two bilayer hBN domains with AB (pink region) and AA' (blue region) stacking orders, with the corresponding correlated spatial map of the second-harmonic generation (SHG) intensity. **c** | In AA' stacked materials, significant SHG occurs only in films with an odd number of layers, with the SHG output nominally insensitive to the number of odd layers within the atomic limit (left). However, for AB stacked materials, SHG is substantial even in bilayers, and much stronger than the emission from an hBN monolayer (right). a.u., arbitrary units. Panels **a** and **b** are adapted with permission from REF.[17], ACS. Panel **c** is adapted with permission from REF.[18], ACS.

the atomic-scale or nano-scale emitter. For an atomic dipole, the rate of the linear (one-photon) and nonlinear (two-photon) processes scale as $\alpha(a/\lambda)^2$ and $\alpha^2\,(a/\lambda)^4$, respectively, where a is the atomic size and α is the fine constant. Owing to the high modal confinement and exceptionally large optical density of states in the hyperbolic system, significant enhancements of the radiative rate of the two-photon emission could be realized, with total enhancements of up to 10^{11} predicted. In principle, this enhancement can also be observed by placing the two-photon emitter in the near-field proximity of a surface-phonon-polariton thin film or structure as well. Thus, although the implementation of hBN in nonlinear optics is still in its infancy, there appears to be a highly promising future for quantum light sources in the mid-IR.

Deep-UV optoelectronics. The growth of high-quality hBN crystals in 2004 (REF.[13]) renewed interest in hBN for optoelectronics applications in the deep-UV spectral range. In their seminal paper, Kenji Watanabe and Takashi Taniguchi demonstrated UV lasing at 215 nm (REF.[13,112]). They later fabricated a planar-emission compact device equipped with a field-emission array as an excitation source, with stable operation and an output power of 0.2 mW at 225 nm (REF.[113]). Although nitride semiconductors of the AlGaN family are widely used for blue and UV lighting[114], hBN is a newcomer for deep-UV applications, competing with AlN; both materials have a bandgap of ~6 eV. The search for efficient, long-life, solid-state devices as an alternative to conventional spectral lamps in the deep UV is driving intense research that is primarily motivated by chemical and biological applications such as photocatalysis, water purification and sterilization, in addition to non-line-of-sight protocols for short-distance communication in atmospherically disturbed conditions[115].

AlN and hBN have very different optoelectronic properties. AlN is a wurtzite semiconductor with a direct bandgap. However, its excitonic fine structure imposes severe limitations on its use as a bright source in the deep UV. This is due to the fact that the fundamental optical transition of AlN is polarized along the *c*-axis, a detrimental feature for vertical surface-emitting devices[116]. By contrast, hBN is a lamellar compound in which the weak interlayer van der Waals forces and the strong in-plane covalent bonds result in an indirect bandgap. The indirect bandgap would appear to be in contradiction with the bright emission observed in the deep UV[112], as this is a feature usually attributed to direct-gap semiconductors. This led to the initial misinterpretation of hBN as a direct bandgap material and sparked a long, controversial debate concerning its electronic structure. The puzzle of bright, deep-UV emission in hBN was recently resolved by photoluminescence induced via two-photon excitation[16], which revealed the full set of emission lines (FIG. 6a). These lines correspond to phonon-assisted optical transitions; the indirect nature of the bandgap requires phonon emission to fulfill momentum conservation during carrier recombination. The deep-UV optoelectronic properties of hBN were further illuminated[23,117] by the discovery that the position of the phonon-assisted emission peaks in monoisotopic samples depends on mass (FIG. 6b) and by the polarization selection rules dictated by the phonon symmetries (FIG. 6c). A key property of hBN is its very peculiar indirect bandgap configuration: the conduction band minimum sits at the M point of the first Brillouin zone, whereas the valence band maximum is located in the neighbourhood of the K point[118–122] (BOX 1). This is a major difference from the configuration of cubic semiconductors such as diamond, silicon and germanium, as their valence band maxima are located at the zone centres (Γ). Phonon-assisted recombination in hBN involves phonons with a wavevector corresponding to Γ–T (T sits in the middle of the line Γ–K; BOX 1) and not at the Brillouin zone edge, as occurs in indirect cubic semiconductors. The indirect bandgap at 5.95 eV in hBN was directly observed by electron energy loss spectroscopy (EELS), in which electrons excited the hBN crystal with the same momentum as phonons at T points[123]. This unusual band structure results in unique optoelectronic properties, such as an influence of the finite group velocity of phonons on the UV response, low phonon group velocities at the T points and narrow emission lines of the phonon replicas[124]. Moreover, the phonon replicas in hBN consist of sharp resonances with linewidths of a

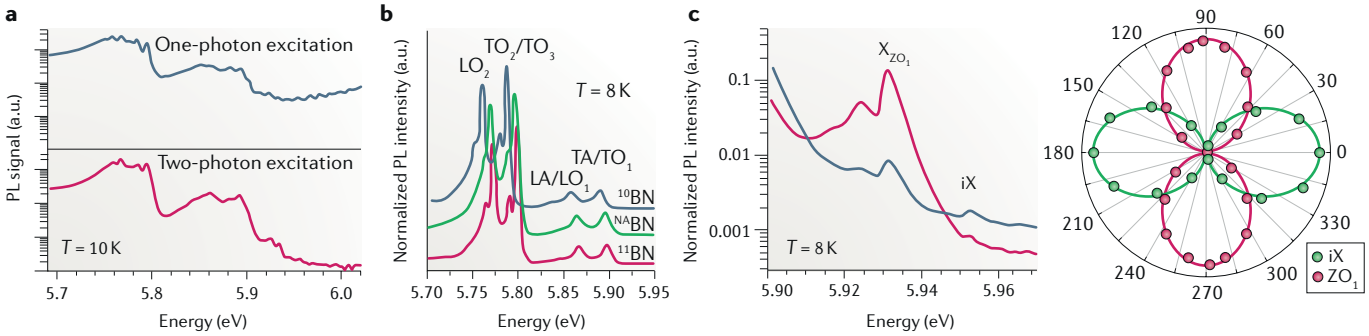

Fig. 6 | **Phonon-assisted recombination in hBN. a** | Photoluminescence (PL) spectra of hexagonal boron nitride (hBN) at 10 K for one-photon excitation at 6.3 eV (top) and for two-photon excitation at 3.03 eV (bottom). The suppression of the laser stray light by two-photon excitations reveals the full series of emission lines near the bandgap of hBN. **b** | PL spectra of hBN as a function of isotopic composition for ^{10}BN, ^{NA}BN (natural BN) and ^{11}BN at 8 K. The labels indicate the phonon modes involved in phonon-assisted recombination. **c** | PL spectra at 8 K for a linearly polarized detection, either parallel (red) or perpendicular (grey) to the *c*-axis, for an emission wavevector *k* perpendicular to the *c*-axis, in the energy range of the fundamental indirect exciton iX around 5.95 eV (left). Polar plot of the PL intensity of the ZO_1 phonon replica and iX line as a function of polarization angle for an emission wavevector *k* perpendicular to the *c*-axis (right). For the ZO_1 phonon replica, the dipole is parallel to the *c*-axis as a result of the atomic vibrations along the *c*-axis for the ZO_1 phonon mode, whereas the dipole of the indirect exciton iX lies in the plane of the hBN layers. a.u., arbitrary units. Panel **a** is adapted from REF.[16], Springer Nature Limited. Panel **b** is adapted from REF.[23], Springer Nature Limited. Panel **c** is adapted from REF.[117], CC-BY-3.0.

few millielectronvolts, instead of the broad resonances characteristic of cubic semiconductors[16].

The bright, deep-UV emission of hBN is due to the strong coupling of the exciton–phonon interactions. Although predicted by Yutaka Toyozawa 60 years ago[125], this was not experimentally observed until 2017 (REF.[126]), when an emission spectrum displaying the two required signatures for a phonon-assisted broadening in the strong-coupling regime — a Gaussian emission lineshape and a square-root temperature dependence of the excitonic linewidth — was observed. Owing to the efficient exciton–phonon interactions, in hBN, the phonon-assisted recombination occurs on a sub-nanosecond timescale[112,127–130]; thus, it is fast enough to bypass nonradiative relaxation. This, in turn, enables the intense deep-UV emission reported from hBN. The internal quantum efficiency is estimated to be up to 40%, close to values typical of direct bandgap semiconductors[131].

For deep-UV lighting, hBN emerges as an active material with outstanding properties. Although direct bandgap semiconductors have the advantage of having high internal quantum efficiencies, reabsorption of the emitted photons severely reduces the efficiency of photon extraction. Conversely, indirect bandgap semiconductors typically display low internal quantum efficiencies owing to the slow phonon-assisted recombination. This well-known dilemma in the early days of light-emitting diode (LED) research was resolved by the invention of quantum wells with direct bandgap, in which the photons emitted from the wells are transmitted by the barriers, making the issue of reabsorption irrelevant. However, with the exceptionally large bandgaps associated with deep-UV emitters, the identification of materials with sufficiently large bandgap barriers becomes increasingly problematic. hBN exhibits high photon extraction efficiencies due to the Stokes shift between phonon-assisted emission and absorption processes, which makes this material an attractive alternative in this application space. Thus, from the perspective of current deep-UV optoelectronics with its quest for suitable active materials, bulk hBN combines the respective advantages of indirect and direct bandgap semiconductors, providing high extraction efficiency and, strikingly, high internal quantum efficiency. These novel properties are motivating intense theoretical investigations in order to include the coupling of phonons together with excitonic effects in ab initio calculations[132,133] and, thus, to understand the origin of the exceptional characteristics exhibited by hBN in the deep UV.

Research into hBN also offers the opportunity to further link nitride compounds and 2D crystals. Up until recently, there remained the open question of the theoretically predicted transition from an indirect to a direct bandgap in hBN at monolayer thicknesses[120,134]. However, very recently this direct bandgap crossover was demonstrated for hBN at the monolayer limit[135]. TMDs provide generic examples of this effect in 2D materials[136], whereas 2D GaN retains its direct bandgap at the monolayer scale with a quantum-confined gap of ~5 eV (REF.[137]). Yet, to date, only cathodoluminescence measurements of six-monolayer hBN have been reported[138]. Thus, measurements of hBN monolayers are still absent, leaving this issue unresolved. Intercalation of foreign atoms could be a route for enhancing the light–matter interaction by changing the nature of the bandgap from indirect to direct upon increasing the interlayer spacing. This is far from trivial but is related to the experimental measurement of a redshift of the bandgap of hBN under compressive hydrostatic pressure[139]. Intercalation would act as a tensile pressure, changing the nature of the bandgap from indirect to direct, in agreement with accurate theoretical predictions[140].

Growth methods

Many applications, such as the four research areas highlighted above, will require hBN samples with high structural perfection and low residual impurity concentrations. Grain boundaries, dislocations and impurities introduce energy levels and charge-scattering centres that can unfavourably alter the electronic and optical properties of hBN in uncontrolled ways. However, from a baseline of high-quality, low-residua l-impurity-concentration hBN, the alteration of these properties could instead be controlled by introducing defects and impurities into the material either to achieve specific properties or to retain the inherent properties of the native lattice. Drawing on analogies from other device materials, processes for bulk crystal growth, epitaxy, in situ doping, etching and metallization need to be developed for hBN if this material is to be implemented in advanced applications.

Bulk crystals of hBN cannot be grown from the melt owing to its extremely high melting temperature, estimated at 3,370 K (REF.[141]). Thus, hBN crystals are grown from solutions that can dissolve both boron and nitrogen. Solution-grown crystals offer hBN with the highest structural quality currently available, because they are produced in processes approaching thermodynamic equilibrium and are not constrained by a substrate. Taniguchi and Watanabe[24] identified $Ba_3B_2N_4$ as a good solvent for crystal growth, because it produces hBN with low concentrations (less than 10^{18} cm^{-3}) of the primary impurities, carbon and oxygen. However, very high nitrogen pressures (4–5 GPa) are required to keep the solvent from decomposing. The crystals have excellent structural quality, exhibiting very smooth surfaces (roughness of 70 pm)[7], narrow Raman spectral peaks (≤8 cm^{-1}) and high optical quality (strong UV emission at 5.8 eV). However, the required extremely high pressures are difficult to achieve in volumes larger than 100 ml, which has limited the size of the hBN crystals that this technique can produce. Nevertheless, the crystal sizes have been sufficient for exploring the fundamental properties of hBN across a broad range of scientific lines of inquiry and for identifying the plethora of potential applications of hBN. Indeed, hBN crystals produced at high pressure have been the material of choice for many hBN studies requiring the best quality materials.

Recognizing that hBN is the stable polymorph of boron nitride at low pressures, nickel and molybdenum mixtures, and then nickel and chromium mixtures, were developed[142,143] to serve as solvents for hBN crystal growth near atmospheric pressure. Nickel is a good solvent for boron, while molybdenum and chromium are good solvents for nitrogen. Of these two, the nickel–chromium mixture has a much higher nitrogen solubility and is, thus, capable of producing a larger area and thicker hBN crystals (up to 100 μm thick)[143]. Strong cathodoluminescence emission at 5.8 eV demonstrated the high quality of crystals produced with this solvent. An iron–chromium mixture is also a viable solvent[144], with the advantage that iron is less expensive than nickel and is commercially available with lower carbon concentrations (typically less than 5 ppm, versus >100 ppm for nickel).

In an alternative bulk growth approach, hBN crystals were grown using pure boron instead of the hot-pressed boron nitride source previously used[145]. Pure boron is available with lower residual impurity concentrations than hot-pressed boron nitride and, thus, has the potential to produce higher-purity hBN crystals. Furthermore, pure boron is available as single isotopes (that is, as isotopically pure hBN, with both ^{10}B and ^{11}B reported[22,23]), enabling the growth of monoisotopic hBN crystals. The resulting hBN crystal flakes are transparent and colourless and have areas of several square millimetres (FIG. 7a). Compared with hBN with its natural boron isotope distribution (20% ^{10}B and 80% ^{11}B), monoisotopic hBN crystals exhibit thermal conductivities more than 40% higher[146] and phonon lifetimes more than three times longer[22,147]. These characteristics make monoisotopic hBN crystals the preferred choice for metasurfaces and nanophotonics[22,52,57,62]. In addition, ^{10}B-enriched hBN is well suited for neutron detectors, owing to the high thermal neutron capture cross-section (>3,800 barns) of ^{10}B, which is among the highest of any elemental isotope[148].

Epitaxial deposition of hBN is currently being intensely researched because of its ability to produce large-area hBN layers with controlled thickness and abrupt doping and compositional transitions[149,150]. Whereas producing atomically thin layers of hBN from bulk crystals requires mechanical exfoliation, which inevitably reduces the flake size with respect to the original crystal domain and/or induces chemical contamination, optimized deposition techniques can be self-limiting, producing single atomic layers of hBN. Deposition by both CVD[25,149] and MBE[26,27,151] have been reported. Research into these methods is focused on the impact of reactants, process conditions (temperature, time and reactant flux rates) and choice of substrate (metals, sapphire or silicon) on the initial nucleation, growth, coalescence, uniformity of thickness, and grain and domain size. However, the challenges facing all heteroepitaxial growth processes arise, including reactions with the substrate and mismatches of crystal symmetries, lattice constants and coefficients of thermal expansion between film and substrate. Therefore, buffer layers, such as AlN on sapphire, have been investigated to improve the quality of the subsequently deposited hBN layer[152]. Changes in the structural and electrical properties of hBN following the addition of silicon[153] and magnesium[154] dopants have also been studied.

In general, deposition on polycrystalline metals used as templates for CVD growth produces materials with relatively small grain size, typically less than 100 μm (REF.[149]). Grain sizes can be increased by ensuring that the metal substrate is smooth and by limiting the initial nucleation of hBN. Recently, the grain size limitation was circumvented by depositing hBN on a flat surface of molten gold[155] (FIG. 7b). In that work, very-large-area monolayers (at least several square millimetres) of hBN were obtained. Surface diffusion of the elements was favoured owing to the limited solubility of boron and nitrogen in the molten gold. The process parameters were optimized so that the initially forming hBN nuclei were uniformly thick and equal in shape and area. With continued growth, these nuclei rearranged

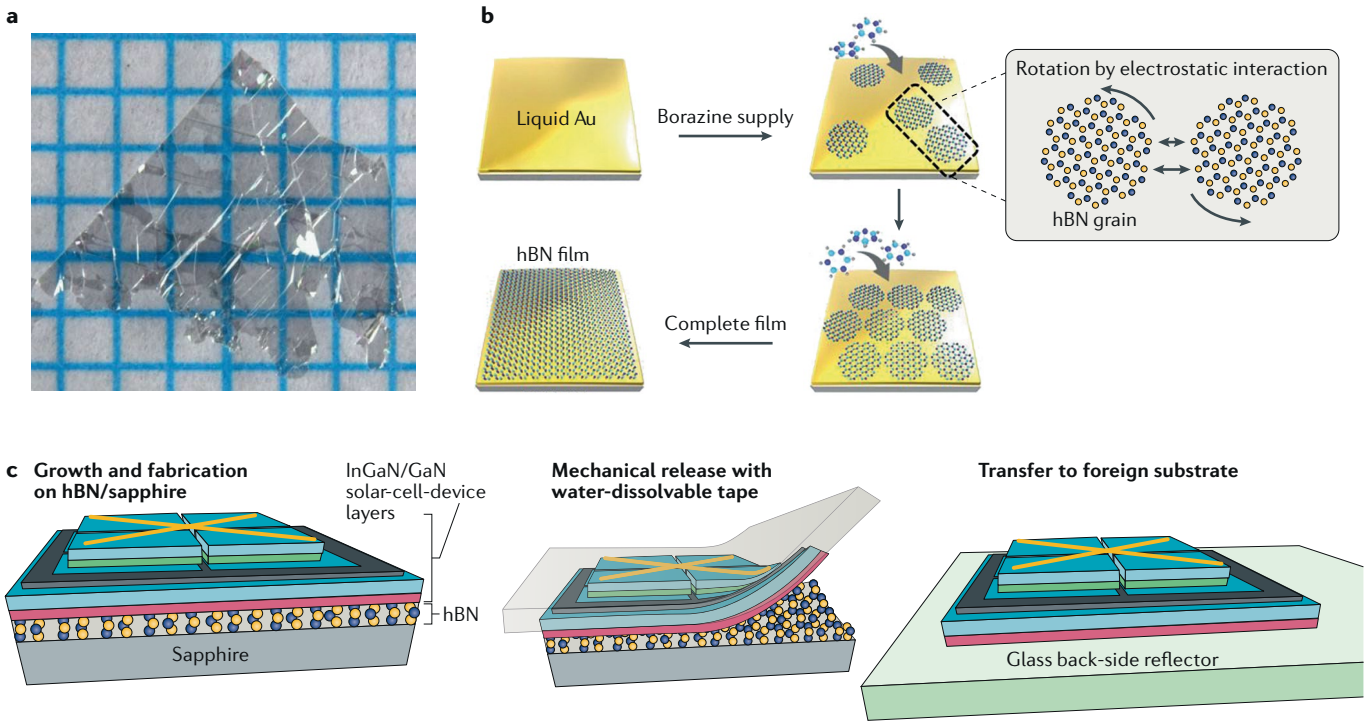

Fig. 7 | **Methods for growing hBN. a** | Photograph of a pure hexagonal boron nitride (hBN) flake grown from a nickel–chromium solution. The grid size is 1 mm x 1 mm and the flake is 15 μm thick. **b** | During chemical vapour deposition of hBN on molten gold using borazine, the individual grains rearrange owing to electrostatic interactions to produce a highly ordered layer. **c** | An epitaxial layer of InGaN grown on an hBN template deposited on a sapphire substrate can be easily removed owing to the weak layer–layer chemical bonding. The exfoliated layer can then be transferred to another substrate[159]. Panel **b** is adapted with permission from REF.[155], AAAS. Panel **c** is adapted with permission from REF.[159], ACS.

to eliminate grain boundaries as they merged to form a continuous hBN layer, a process the authors referred to as self-collimation. Subsequently, these hBN monolayers were employed as a substrate for highly aligned, single-crystal layers of graphene and WS_2 (REF.[155]). Similar results were obtained using liquid copper as the substrate[156], offering the promise of optimized, thin-film, large-area growth methods in the near future.

An additional unique application of deposited hBN films is their use as a release layer. To this end, hBN was first deposited on sapphire, then GaN-based device layers were deposited on top[157,158]. Because the GaN layers are only weakly bonded to the hBN, they are easily peeled off from the substrate and transferred onto a thermally conductive handle substrate that can better dissipate heat or provide a flexible substrate[159] (FIG. 7c). Following this procedure allows the sapphire substrate to be reused, significantly reducing the growth costs of the devices. In a similar vein, wafer-scale, free-standing 2D materials (including hBN) can be realized with a layer-resolved splitting technique. This method could be advantageous also for other applications, such as chemical and isotope separation with atomically thin membranes[160].

To date, research into deposited hBN has focused on control of the film stoichiometry, layer thickness and domain sizes. The composition of the films, their structural quality and their optical properties are typically characterized by X-ray photoelectron spectroscopy, transmission electron microscopy, X-ray powder diffraction, AFM (typically, the roughness is greater than 0.3 nm and increases with layer thickness), Raman spectroscopy and photoluminescence. Assessments of layer purity and crystalline perfection have generally been missing, with the exception of experiments based on Raman spectroscopy, which is commonly employed for quantifying material quality. For deposited hBN, the Raman peak positions are often shifted (indicating strain) and broadened (full width at half maximum between 12 and 20 cm^{-1})[161] compared with those of bulk hBN (<8 cm^{-1})[22]. The hBN quality can change with the layer thickness: the BN layer polytype was shown to change from hexagonal to rhombohedral at ~4 nm on sapphire substrates[153]. Thus, future research should focus on improving the size of hBN crystals, quantifying the effects of impurities, improving control of structural quality and introducing p-type and n-type dopants with precise control.

van der Waals heterostructures

hBN is instrumental for controlling material properties through van der Waals epitaxy. 2D interfaces are crucial for the performance of the ubiquitous field-effect transistor and also give rise to new emergent phenomena, such as the quantum Hall effect. In conventional solids, lattice matching and other considerations limit the materials that can be combined by epitaxial growth. By contrast, van der Waals epitaxy (assembly) eliminates

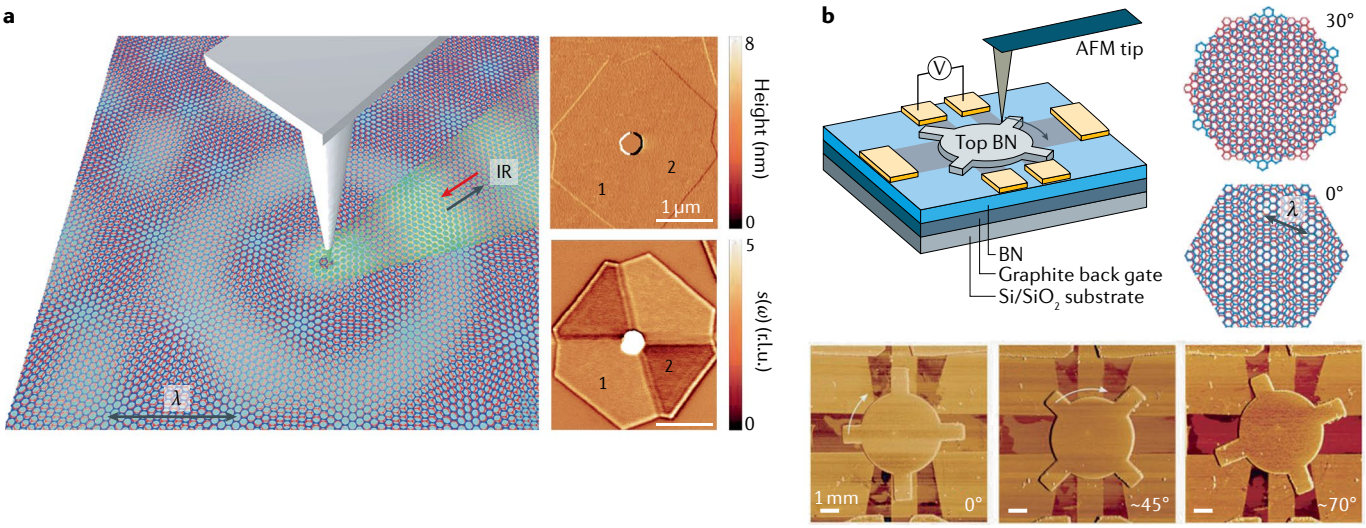

Fig. 8 | **Moiré heterostructures incorporating hBN. a** | Schematic of scanning plasmon interferometry experiments on graphene on hexagonal boron nitride (hBN) with a moiré superlattice pattern. The red and black arrows display the directions of incident and back-scattered IR light, respectively. Concentric circles illustrate polariton waves launched by an atomic force microscope (AFM) tip, which is illuminated by a laser. The waves are reflected by the graphene edges, resulting in interference between the launched and back-reflected plasmon polariton waves. Thus, nano-IR measurements visualize polaritonic standing waves in hBN and other 2D materials. Top right: AFM topography of the sample. Bottom right: nano-IR scattering amplitude at a frequency of $\omega = 990\ cm^{-1}$. Boundaries between plain graphene (region 2) and moiré-patterned graphene (region 1) also act as plasmonic reflectors. **b** | Schematic cartoon of the device structure and experimental technique for realizing rotatable heterostructures. Bottom frames: AFM images of a device showing three different orientations of the top hBN disk. The images were acquired by the same AFM used to rotate the hBN layer. Top right: schematic illustration of the moiré superlattice arising between graphene (red) and BN (blue) as a function of the rotation angle. r.l.u., reciprocal lattice units. Panel **a** is adapted from REF.[19], Springer Nature Limited. Panel **b** is adapted with permission from REF.[187], AAAS.

crystal lattice matching as a prerequisite for interface engineering, thereby allowing the integration of atomically layered materials with arbitrary lattices and widely different properties[4,5,7,162,163].

The interface of graphene with hBN is arguably the most studied system. These two hexagonal layered materials have a lattice mismatch of approximately 1.8%. Transport and tunnelling microscopy studies of graphene/hBN heterostructures have uncovered a broad range of unusual properties, including exotic quantum Hall features, the fractional quantum Hall effect, the quantum spin Hall effect, an insulating state at the charge neutrality point, Coulomb drag, Hofstadter quantization, magnetic focusing[164] and ballistic propagation of surface plasmon polaritons[10]; these effects are summarized in several comprehensive review articles[165,166].

The role of boron nitride in graphene/hBN heterostructures goes beyond simply providing a means for the elimination of extrinsic effects. The hBN can create a superlattice potential (the moiré potential) that acts on charge carriers in graphene, resulting in a controlled modification of the electronic structure of graphene[167–171]. The Hofstadter quantization is a spectacular example of the modification of the electronic response by the moiré potential. Optical experiments involving graphene/hBN are sparse, a consequence of the experimental complexity of measurements involving small specimens. IR microscopy of aligned graphene/hBN has uncovered new spectral features attributable to modified electronic structure[172]. A study of the propagation of surface plasmon polaritons in monolayer graphene epitaxially grown on hBN revealed that the surface plasmon polariton wavelength and losses are both modified in regions in which graphene and hBN form a moiré superlattice[19]. The analysis of images detailing surface plasmon polariton propagation in such structures allowed the reconstruction of the electronic structure of the superlattice. The results (FIG. 8a) confirmed the theoretical prediction of the existence of so-called morphed plasmons, surface plasmon polaritons originating from the concerted response of intraband Dirac quasiparticles and interband processes[173].

Extremely rich, electronic effects have been predicted for moiré superlattices formed by two hBN monolayers. Density functional calculations[174] predict that, in twisted bilayer hBN, multiple flat bands emerge. Provided hBN moiré superlattices can be doped, the emergence of correlated electronic phases, including superconductivity, is expected. The same work also predicted the formation of relatively narrow electronic bands within the wide bandgap of common hBN.

A unique control knob specific to van der Waals systems is the twist angle α between adjacent layers (FIG. 8b). Varying α produces long-range moiré patterns, with a continuously tunable periodicity (ranging from tens of nanometres to ~1 μm) that radically modifies the electronic structure and materials properties[21,169,175–185]. To fully exploit the opportunities offered by van der Waals moiré

interfaces, it is imperative to implement in operando control of the twist angle. The technical feasibility of this task has been demonstrated[186,187]. Rich, nanoscale phenomena occurring in rotatable metastructures can now be realized using scanning probe methods[20]; this promises new physical insights into the atomic-scale electronic interactions observed in these moiré superlattices.

Outlook

hBN is a promising material for a broad range of applications. In this Review, we have highlighted key advances, including IR nanophotonics, SPEs spanning the range from visible to near-IR, nonlinear optical phenomena, UV emitters and moiré superlattices comprising hBN and other van der Waals materials. Specifically, we discussed the current state-of-the-art in the implementation of the natural hyperbolic properties of hBN for IR applications, including on-chip photonics and hyperlensing, and in the understanding of the origin of room-temperature, single-photon emission, of the role of hBN stacking order in modifying its nonlinear response and of the counterintuitive, bright, deep-UV emission from the indirect bandgap of hBN. In all these areas, significant progress has been made; however, there are knowledge gaps that must be filled and advancements in materials development that must be made before these potential applications can be translated into commercial success. One significant outstanding challenge lies in the further development of large-area growth and/or deposition of the low-defect, high-quality hBN required for transitioning these and other applications of hBN to the commercial realm.

Published online 12 July 2019

1. Novoselov, K. S. et al. Electric field effect in atomically thin carbon films. *Science* **306**, 666–669 (2004).
2. Novoselov, K. S. et al. Two-dimensional gas of massless Dirac fermions in graphene. *Nature* **438**, 197–200 (2005).
3. Zhang, Y., Tan, Y.-W., Stormer, H. L. & Kim, P. Experimental observation of the quantum Hall effect and Berry's phase in graphene. *Nature* **438**, 201–204 (2005).
4. Novoselov, K. S., Mishchenko, A., Carvalho, A. & Castro Neto, A. H. 2D materials and van der Waals heterostructures. *Science* **353**, aac9439 (2016).
5. Geim, A. K. & Grigorieva, I. V. Van der Waals heterostructures. *Nature* **499**, 419–425 (2013).
6. Kretinin, A. et al. Electronic properties of graphene encapsulated with different two-dimensional atomic crystals. *Nano Lett.* **14**, 3270–3276 (2014).
7. Dean, C. R. et al. Boron nitride substrates for high-quality graphene electronics. *Nat. Nanotechnol.* **5**, 722–726 (2010).
8. Lee, G.-H. et al. Flexible and transparent MoS_2 field-effect transistors on hexagonal boron-nitride-graphene heterostructures. *ACS Nano* **7**, 7931–7936 (2013).
9. Woessner, A. et al. Highly confined low-loss plasmons in graphene-boron nitride heterostructures. *Nat. Mater.* **14**, 421–425 (2015).
10. Ni, G. X. et al. Fundamental limits to graphene plasmonics. *Nature* **557**, 530–533 (2018).
11. Dai, S. et al. Tunable phonon polaritons in atomically thin van der Waals crystals of boron nitride. *Science* **343**, 1125–1129 (2014).
12. Caldwell, J. D. et al. Sub-diffractional volume-confined polaritons in the natural hyperbolic material hexagonal boron nitride. *Nat. Commun.* **5**, 5221 (2014).
13. Watanabe, K., Taniguchi, K. & Kanda, H. Direct-bandgap properties and evidence for ultraviolet lasing of hexagonal boron nitride single crystals. *Nat. Mater.* **3**, 404–409 (2004).
14. Dai, S. et al. Graphene on hexagonal boron nitride as a tunable hyperbolic metamaterial. *Nat. Nanotechnol.* **10**, 682–686 (2015).
15. Tran, T.-T. D., Bray, V. W., Ford, M. J., Toth, M. & Aharonovich, I. Quantum emission from hexagonal boron nitride monolayers. *Nat. Nanotechnol.* **11**, 37–41 (2016).
16. Cassabois, G., Valvin, P. & Gil, B. Hexagonal boron nitride is an indirect bandgap semiconductor. *Nat. Photonics* **10**, 262–266 (2016).
17. Kim, C.-J. et al. Stacking order dependent second harmonic generation and topological defects in h-BN bilayers. *Nano Lett.* **13**, 5660–5665 (2013).
18. Li, Y. et al. Probing symmetry properties of few-layer MoS_2 and h-BN by optical second harmonic generation. *Nano Lett.* **13**, 3329–3333 (2013).
19. Ni, G. X. et al. Plasmons in graphene moiré superlattices. *Nat. Mater.* **14**, 1217–1222 (2015).
20. Sunku, S. S. et al. Photonic crystals for nano-light in moiré graphene superlattices. *Science* **362**, 1153–1156 (2018).
21. Yu, H. Y., Liu, G. B., Tang, J. J., Xu, X. D. & Yao, W. Moiré excitons: from programmable quantum emitter arrays to spin-orbit-coupled artificial lattices. *Sci. Adv.* **3**, e1701696 (2017).
22. Giles, A. J. et al. Ultra-low-loss polaritons in isotopically pure boron nitride. *Nat. Mater.* **17**, 134–139 (2018).
23. Vuong, T. Q. P. et al. Isotope engineering of van der Waals interactions in hexagonal boron nitride. *Nat. Mater.* **17**, 152–158 (2018).
24. Taniguchi, T. & Watanabe, K. Synthesis of high-purity boron nitride single crystals under high pressure by using Ba-BN solvent. *J. Cryst. Growth* **303**, 525–529 (2007).
25. Du, X. Z., Li, J., Lin, J. Y. & Jiang, H. X. The origins of near band-edge transitions in hexagonal boron nitride epilayers. *Appl. Phys. Lett.* **108**, 052106 (2016).
26. Cho, Y.-J. et al. Hexagonal boron nitride tunnel barriers grown on graphite by high temperature molecular beam epitaxy. *Sci. Rep.* **6**, 34474 (2016).
27. Vuong, T. Q. P. et al. Deep ultraviolet emission in hexagonal boron nitride grown by high-temperature molecular beam epitaxy. *2D Mater.* **4**, 021023 (2017).
28. Folland, T. G., Nordin, L., Wasserman, D. & Caldwell, J. D. Probing polaritons in the mid- to far-infrared. *J. Appl. Phys.* **125**, 191102 (2019).
29. Maier, S. A. *Plasmonics: Fundamentals and Applications* (Springer-Verlag, 2007).
30. Caldwell, J. D. et al. Low-loss, infrared and terahertz nanophotonics with surface phonon polaritons. *Nanophotonics* **4**, 44–68 (2015).
31. Basov, D. N., Fogler, M. M. & Garcia de Abajo, F. J. Polaritons in van der Waals materials. *Science* **354**, aag1992 (2017).
32. Low, T. et al. Polaritons in layered two-dimensional materials. *Nat. Mater.* **16**, 182–194 (2017).
33. Xu, X. G. et al. One-dimensional surface phonon polaritons in boron nitride nanotubes. *Nat. Commun.* **5**, 4782 (2014).
34. Caldwell, J. D. & Novoselov, K. S. Mid-infrared nanophotonics. *Nat. Mater.* **14**, 364–365 (2015).
35. Ni, G. X. et al. Ultrafast optical switching of infrared plasmon polaritons in high-mobility graphene. *Nat. Photonics* **10**, 244–247 (2016).
36. Adachi, S. *Optical Properties of Crystalline and Amorphous Semiconductors: Materials and Fundamental Principles* 33–61 (Springer Science+Business Media, 1999).
37. Poddubny, A., Iorsh, I., Belov, P. & Kivshar, Y. Hyperbolic metamaterials. *Nat. Photonics* **7**, 948–957 (2013).
38. Caldwell, J. D., Vurgaftman, I. & Tischler, J. G. Probing hyperbolic polaritons. *Nat. Photonics* **9**, 638–640 (2015).
39. Yoxall, E. et al. Direct observation of ultraslow hyperbolic polariton propagation with negative phase velocity. *Nat. Photonics* **9**, 674–678 (2015).
40. Autore, M. et al. Boron nitride nanoresonators for phonon-enhanced molecular vibrational spectroscopy at the strong coupling limit. *Light Sci. Appl.* **7**, 17172 (2018).
41. Dai, S. et al. Subdiffractional focusing and guiding of polaritonic rays in a natural hyperbolic material. *Nat. Commun.* **6**, 6963 (2015).
42. Guo, Y., Newman, W., Cortes, C. L. & Jacob, Z. Applications of hyperbolic metamaterial substrates. *Adv. Optoelectron.* **2012**, 452502 (2012).
43. Liu, Z., Lee, H., Xiong, Y., Sun, C. & Zhang, X. Far-field optical hyperlens magnifying sub-diffraction-limited objects. *Science* **315**, 1686 (2007).
44. Argyropoulos, C., Estakhri, N. M., Monticone, F. & Alu, A. Negative refraction, gain and nonlinear effects in hyperbolic metamaterials. *Opt. Express* **21**, 15037–15047 (2013).
45. Hoffman, A. J. et al. Negative refraction in semiconductor metamaterials. *Nat. Mater.* **6**, 946–950 (2007).
46. Shalaev, V. M. et al. Negative index of refraction in optical metamaterials. *Opt. Lett.* **30**, 3356–3358 (2005).
47. Lin, X. et al. All-angle negative refraction of highly squeezed plasmon and phonon polaritons in graphene-boron nitride heterostructures. *Proc. Natl Acad. Sci. USA* **114**, 6717–6721 (2017).
48. Qian, C. et al. Multifrequency superscattering from subwavelength hyperbolic structures. *ACS Photonics* **5**, 1506–1511 (2018).
49. Cortes, C. L., Newman, W., Molesky, S. & Jacob, Z. Quantum nanophotonics using hyperbolic metamaterials. *J. Opt.* **14**, 063001 (2012).
50. Giles, A. J. et al. Imaging of anomalous internal reflections of hyperbolic phonon-polaritons in hexagonal boron nitride. *Nano Lett.* **16**, 3858–3865 (2016).
51. Li, P. et al. Hyperbolic phonon-polaritons in boron nitride for near-field optical imaging and focusing. *Nat. Commun.* **6**, 7507 (2015).
52. Folland, T. G. et al. Probing hyperbolic polaritons using infrared attenuated total reflectance micro-spectroscopy. *MRS Commun.* **8**, 1418–1425 (2018).
53. Dai, S. et al. Internal nanostructure diagnosis with hyperbolic phonon polaritons in hexagonal boron nitride. *Nano Lett.* **18**, 5205–5210 (2018).
54. Brown, L. V. et al. Nanoscale mapping and spectroscopy of nonradiative hyperbolic modes in hexagonal boron nitride nanostructures. *Nano Lett.* **18**, 1628–1636 (2018).
55. Sun, Z., Gutierrez-Rubio, A., Basov, D. N. & Fogler, M. M. Hamiltonian optics of hyperbolic polaritons in nanogranules. *Nano Lett.* **15**, 4455–4460 (2015).
56. Li, P. et al. Reversible optical switching of highly confined phonon-polaritons with an ultrathin phase-change material. *Nat. Mater.* **15**, 870–875 (2016).
57. Folland, T. G. et al. Reconfigurable infrared hyperbolic metasurfaces using phase change materials. *Nat. Commun.* **9**, 4371 (2018).
58. Michel, A.-K. U. et al. Using low-loss phase-change materials for mid-infrared antenna resonance tuning. *Nano Lett.* **13**, 3470–3475 (2013).
59. Dunkelberger, A. D. et al. Active tuning of surface phonon polariton resonances via carrier photoinjection. *Nat. Photonics* **12**, 50–56 (2018).
60. Spann, B. T. et al. Photoinduced tunability of the reststrahlen band in 4H-SiC. *Phys. Rev. B* **93**, 085205 (2016).
61. Caldwell, J. D. et al. Atomic-scale photonic hybrids for mid-infrared and terahertz nanophotonics. *Nat. Nanotechnol.* **11**, 9–15 (2016).

62. Li, P. et al. Infrared hyperbolic metasurface based on nanostructured van der Waals materials. *Science* **359**, 892–896 (2018).
63. Wang, T. et al. Phonon-polaritonic bowtie nanoantennas: controlling infrared thermal radiation at the nanoscale. *ACS Photonics* **4**, 1753–1760 (2017).
64. Adato, R. et al. Ultra-sensitive vibrational spectroscopy of protein monolayers with plasmonic nanoantenna arrays. *Proc. Natl Acad. Sci. USA* **106**, 19227–19232 (2009).
65. Ma, W. et al. In-plane anisotropic and ultra-low-loss polaritons in a natural van der Waals crystal. *Nature* **562**, 557–562 (2018).
66. Zheng, Z. et al. Highly confined and tunable hyperbolic phonon polaritons in van der Waals semiconducting transition metal oxides. *Adv. Mater.* **30**, 1705318 (2018).
67. Folland, T. G. & Caldwell, J. D. Precise control of infrared polarization using crystal vibrations. *Nature* **562**, 499–501 (2018).
68. Tran, T. T., Bray, K., Ford, M. J., Toth, M. & Aharonovich, I. Quantum emission from hexagonal boron nitride monolayers. *Nat. Nanotechnol.* **11**, 37–41 (2016).
69. Tran, T. T. et al. Robust multicolor single photon emission from point defects in hexagonal boron nitride. *ACS Nano* **10**, 7331–7338 (2016).
70. Jungwirth, N. R. et al. Temperature dependence of wavelength selectable zero-phonon emission from single defects in hexagonal boron nitride. *Nano Lett.* **16**, 6052–6057 (2016).
71. Exarhos, A. L., Hopper, D. A., Grote, R. R., Alkauskas, A. & Bassett, L. C. Optical signatures of quantum emitters in suspended hexagonal boron nitride. *ACS Nano* **11**, 3328–3336 (2017).
72. Shotan, Z. et al. Photoinduced modification of single-photon emitters in hexagonal boron nitride. *ACS Photonics* **3**, 2490–2496 (2016).
73. Abdi, M., Chou, J.-P., Gali, A. & Plenio, M. B. Color centers in hexagonal boron nitride monolayers: a group theory and ab initio analysis. *ACS Photonics* **5**, 1967–1976 (2018).
74. Tawfik, S. A. et al. First-principles investigation of quantum emission from hBN defects. *Nanoscale* **9**, 13575–13582 (2017).
75. Martínez, L. J. et al. Efficient single photon emission from a high-purity hexagonal boron nitride crystal. *Phys. Rev. B* **94**, 121405 (2016).
76. Tran, T. T. et al. Quantum emission from defects in single-crystalline hexagonal boron nitride. *Phys. Rev. Appl.* **5**, 034005 (2016).
77. Chejanovsky, N. et al. Quantum light in curved low dimensional hexagonal boron nitride systems. *Sci. Rep.* **7**, 14758 (2017).
78. Koperski, M., Nogajewski, K. & Potemski, M. Single photon emitters in boron nitride: more than a supplementary material. *Opt. Commun.* **411**, 158–165 (2018).
79. Hernández-Mínguez, A., Lähnemann, J., Nakhaie, S., Lopes, J. M. J. & Santos, P. V. Luminescent defects in a few-layer *h*-BN film grown by molecular beam epitaxy. *Phys. Rev. Appl.* **10**, 044031 (2018).
80. Mendelson, N. et al. Bottom up engineering of near-identical quantum emitters in atomically thin materials. Preprint at *arXiv* https://arxiv.org/abs/1806.01199 (2019).
81. Stern, H. L. et al. Spectrally resolved photodynamics of individual emitters in large-area monolayers of hexagonal boron nitride. *ACS Nano* **13**, 4548–4547 (2019).
82. Choi, S. et al. Engineering and localization of quantum emitters in large hexagonal boron nitride layers. *ACS Appl. Mater. Interfaces* **8**, 29642–29648 (2016).
83. Ngoc My Duong, H. et al. Effects of high-energy electron irradiation on quantum emitters in hexagonal boron nitride. *ACS Appl. Mater. Interfaces* **10**, 24886–24891 (2018).
84. Proscia, N. V. et al. Near-deterministic activation of room-temperature quantum emitters in hexagonal boron nitride. *Optica* **5**, 1128–1134 (2018).
85. Xu, Z.-Q. et al. Single photon emission from plasma treated 2D hexagonal boron nitride. *Nanoscale* **10**, 7957–7965 (2018).
86. Jungwirth, N. R. & Fuchs, G. D. Optical absorption and emission mechanisms of single defects in hexagonal boron nitride. *Phys. Rev. Lett.* **119**, 057401 (2017).
87. Schell, A. W., Tran, T. T., Takashima, H., Takeuchi, S. & Aharonovich, I. Non-linear excitation of quantum emitters in hexagonal boron nitride multiplayers. *APL Photonics* **1**, 091302 (2016).
88. Wang, Q. et al. Photoluminescence upconversion by defects in hexagonal boron nitride. *Nano Lett.* **18**, 6898–6905 (2018).
89. Bourrellier, R. et al. Bright UV single photon emission at point defects in *h*-BN. *Nano Lett.* **16**, 4317–4321 (2016).
90. Sontheimer, B. et al. Photodynamics of quantum emitters in hexagonal boron nitride revealed by low-temperature spectroscopy. *Phys. Rev. B* **96**, 121202 (2017).
91. Tran, T. T. et al. Resonant excitation of quantum emitters in hexagonal boron nitride. *ACS Photonics* **5**, 295–300 (2018).
92. Dietrich, A. et al. Observation of Fourier transform limited lines in hexagonal boron nitride. *Phys. Rev. B* **98**, 081414 (2018).
93. Konthasinghe, K. et al. Rabi oscillations and resonance fluorescence from a single hexagonal boron nitride quantum emitter. *Optica* **6**, 542–548 (2019).
94. Noh, G. et al. Stark tuning of single-photon emitters in hexagonal boron nitride. *Nano Lett.* **18**, 4710–4715 (2018).
95. Nikolay, N. et al. Very large and reversible Stark-shift tuning of single emitters in layered hexagonal boron nitride. *Phys. Rev. Appl.* **11**, 041001 (2019).
96. Grosso, G. et al. Tunable and high-purity room temperature single-photon emission from atomic defects in hexagonal boron nitride. *Nat. Commun.* **8**, 705 (2017).
97. Xue, Y. et al. Anomalous pressure characteristics of defects in hexagonal boron nitride flakes. *ACS Nano* **12**, 7127–7133 (2018).
98. Tran, T. T. et al. Deterministic coupling of quantum emitters in 2D materials to plasmonic nanocavity arrays. *Nano Lett.* **17**, 2634–2639 (2017).
99. Nguyen, M. et al. Nanoassembly of quantum emitters in hexagonal boron nitride and gold nanospheres. *Nanoscale* **10**, 2267–2274 (2018).
100. Schell, A. W., Takashima, H., Tran, T. T., Aharonovich, I. & Takeuchi, S. Coupling quantum emitters in 2D materials with tapered fibers. *ACS Photonics* **4**, 761–767 (2017).
101. Kim, S. et al. Photonic crystal cavities from hexagonal boron nitride. *Nat. Commun.* **9**, 2623 (2018).
102. Fröch, J. E., Hwang, Y., Kim, S., Aharonovich, I. & Toth, M. Photonic nanostructures from hexagonal boron nitride. *Adv. Opt. Mater.* **7**, 1801344 (2018).
103. Liu, C.-H. et al. Ultrathin van der Waals metalenses. *Nano Lett.* **18**, 6961–6966 (2018).
104. Doherty, M. W. et al. The nitrogen-vacancy colour centre in diamond. *Phys. Rep.* **528**, 1–45 (2013).
105. Toledo, J. R. et al. Electron paramagnetic resonance signature of point defects in neutron-irradiated hexagonal boron nitride. *Phys. Rev. B* **98**, 155203 (2018).
106. Exarhos, A. L., Hopper, D. A., Patel, R. N., Doherty, M. W. & Bassett, L. C. Magnetic-field-dependent quantum emission in hexagonal boron nitride at room temperature. *Nat. Commun.* **10**, 222 (2019).
107. Feng, J. et al. Imaging of optically active defects with nanometer resolution. *Nano Lett.* **18**, 1739–1744 (2018).
108. Comtet, J. et al. Wide-field spectral super-resolution mapping of optically active defects in hexagonal boron nitride. *Nano Lett.* **19**, 2516–2523 (2019).
109. Kianinia, M. et al. All-optical control and super-resolution imaging of quantum emitters in layered materials. *Nat. Commun.* **9**, 874 (2018).
110. Liu, C-h., Zheng, J., Chen, Y., Fryett, T. & Majumdar, A. Van der Waals materials integrated nanophotonic devices [Invited]. *Opt. Mater. Express* **9**, 384–399 (2019).
111. Rivera, N., Rosolen, G., Joannopoulos, J. D., Kaminer, I. & Soljacic, M. Making two-photon processes dominate on-photon processes using mid-IR phonon polaritons. *Proc. Natl Acad. Sci. USA* **114**, 13607–13612 (2017).
112. Watanabe, K. et al. Hexagonal boron nitride as a new ultraviolet luminescent material and its application — fluorescence properties of hBN single-crystal powder. *Diam. Relat. Mater.* **20**, 849–852 (2011).
113. Watanabe, K., Taniguchi, K., Niiyama, T., Miya, K. & Taniguchi, M. Far-ultraviolet plane-emission handheld device based on hexagonal boron nitride. *Nat. Photonics* **3**, 591–594 (2009).
114. Nanishi, Y. Nobel Prize in Physics: the birth of the blue LED. *Nat. Photonics* **8**, 884–886 (2014).
115. Drost, R. J. & Sadler, B. M. Survey of ultraviolet non-line-of-sight communications. *Semicond. Sci. Technol.* **29**, 084006 (2014).
116. Gil, B. *Physics of Wurtzite Nitrides and Oxides* (Springer, 2014).
117. Vuong, T. Q. P. et al. Phonon symmetries in hexagonal boron nitride probed by incoherent light emission. *2D Mater.* **4**, 011004 (2017).
118. Xu, Y.-N. & Ching, W. Y. Calculation of ground-state and optical properties of boron nitrides in the hexagonal, cubic, and wurtzite structures. *Phys. Rev. B* **44**, 7787–7798 (1991).
119. Furthmuller, J., Hafner, J. & Kresse, G. Ab initio calculation of the structural and electronic properties of carbon and boron nitride using ultrasoft pseudopotentials. *Phys. Rev. B* **50**, 15606–15622 (1994).
120. Blase, X., Rubio, A., Louie, S. G. & Cohen, M. L. Quasiparticle band structure of bulk hexagonal boron nitride and related systems. *Phys. Rev. B* **51**, 6868–6875 (1995).
121. Arnaud, B., Lebegue, S., Rabiller, P. & Alouani, M. Huge excitonic effects in layered hexagonal boron nitride. *Phys. Rev. Lett.* **96**, 026402 (2006).
122. Gao, S.-P. Crystal structures and band gap characters of hBN polytypes predicted by dispersion corrected DFT and GW method. *Solid State Commun.* **152**, 1817–1820 (2012).
123. Schuster, R., Habenicht, C., Ahmad, M., Knupfer, M. & Buchner, B. Direct observation of the lowest indirect exciton state in the bulk of hexagonal boron nitride. *Phys. Rev. B* **97**, 041201 (2018).
124. Vuong, T. Q. P. et al. Overtones of interlayer shear modes in the phonon-assisted emission spectrum of hexagonal boron nitride. *Phys. Rev. B* **95**, 045207 (2017).
125. Toyozawa, Y. Theory of line-shapes of the exciton absorption bands. *Progress Theor. Phys.* **20**, 53–81 (1958).
126. Vuong, T. Q. P. et al. Exciton-phonon interaction in the strong-coupling regime in hexagonal boron nitride. *Phys. Rev. B* **95**, 211202(R) (2017).
127. Watanabe, K., Taniguchi, K., Kuroda, T. & Tsuda, O. Time-resolved photoluminescence in band-edge region of hexagonal boron nitride single crystals. *Diam. Relat. Mater.* **17**, 830–832 (2008).
128. Cao, X. K., Clubine, B., Edgar, J. H., Lin, J. Y. & Jiang, H. X. Two-dimensional excitons in three-dimensional hexagonal boron nitride. *Appl. Phys. Lett.* **103**, 191106 (2013).
129. Cassabois, G., Valvin, P. & Gil, B. Intervalley scattering in hexagonal boron nitride. *Phys. Rev. B* **93**, 035207 (2016).
130. Chichibu, S. F., Ishikawa, Y., Kominami, H. & Hara, K. Nearly temperature-independent ultraviolet light emission intensity of indirect excitons in hexagonal BN microcrystals. *J. Appl. Phys.* **123**, 065104 (2018).
131. Schue, L. et al. Direct and indirect excitons with high binding energies in hBN. *Phys. Rev. Lett.* **122**, 067401 (2018).
132. Cannuccia, E., Monserrat, B. & Attaccalite, C. Theory of phonon-assisted luminescence in solids: application to hexagonal boron nitride. *Phys. Rev. B* **99**, 081109(R) (2018).
133. Paleari, F., Miranda, H. P. C., Molina-Sanchez, A. & Wirtz, L. Exciton-phonon coupling in the UV absorption and emission spectra of bulk hexagonal boron nitride. *Phys. Rev. Lett.* **122**, 187401 (2018).
134. Paleari, F. et al. Excitons in few-layer hexagonal boron nitride: Davydov splitting and surface localization. *2D Mater.* **5**, 045017 (2018).
135. Elias, C. et al. Direct band-gap crossover in epitaxial monolayer boron nitride. *Nat. Commun.* **10**, 2639 (2019).
136. Mak, K. F., Lee, C., Hone, J., Shan, J. & Heinz, T. F. Atomically thin MoS_2: a new direct-gap semiconductor. *Phys. Rev. Lett.* **105**, 136805 (2010).
137. Al Balushi, Z. Y. et al. Two-dimensional gallium nitride realized via graphene encapsulation. *Nat. Mater.* **15**, 1166–1171 (2016).
138. Schue, L. et al. Dimensionality effects on the luminescence properties of hBN. *Nanoscale* **8**, 6986–6993 (2016).
139. Akamaru, H., Onodera, A., Endo, T. & Mishima, O. Pressure dependence of the optical-absorption edge of AlN and graphite-type BN. *J. Phys. Chem. Solids* **63**, 887–894 (2002).
140. Koskelo, J. et al. Excitons in van der Waals materials: from monolayer to bulk hexagonal boron nitride. *Phys. Rev. B* **95**, 035125 (2017).
141. Vinogradov, V. L. & Kostanovskii, A. V. Determination of the melting parameters of boron-nitride [in Russian]. *High Temp.* **29**, 901–908 (1991).
142. Kubota, Y., Watanabe, K., Tsuda, O. & Taniguchi, K. Deep ultraviolet light-emitting hexagonal boron nitride synthesized at atmospheric pressure. *Science* **317**, 932–934 (2007).

143. Kubota, Y., Watanabe, K., Tsuda, O. & Taniguchi, K. Hexagonal boron nitride single crystal growth at atmospheric pressure using Ni-Cr solvent. *Chem. Mater.* **20**, 1661–1663 (2008).
144. Liu, S. et al. Large scale growth of high quality hexagonal boron nitride crystals at atmospheric pressure from an iron-chromium flux. *Cryst. Growth Des.* **17**, 4932–4935 (2017).
145. Liu, S. et al. Single crystal growth of millimeter-sized monoisotopic hexagonal boron nitride. *Chem. Mater.* **30**, 6222–6225 (2018).
146. Yuan, C. et al. Modulating the thermal conductivity in hexagonal boron nitride via controlled boron isotope concentration. *Commun. Phys.* **2**, 43 (2019).
147. Cusco, R. et al. Isotopic effects on phonon anharmonicity in layered van der Waals crystals: isotopically pure hexagonal boron nitride. *Phys. Rev. B* **97**, 155435 (2018).
148. Maity, A., Grenadier, S. L., Li, J., Lin, J. Y. & Jiang, H. X. Hexagonal boron nitride neutron detectors with high detection efficiencies. *J. Appl. Phys.* **123**, 044501 (2018).
149. Sun, J. et al. Recent progress in the tailored growth of two-dimensional hexagonal boron nitride via chemical vapour deposition. *Chem. Soc. Rev.* **47**, 4242–4257 (2018).
150. Wang, H.-Z., Zhao, Y., Xie, Y., Ma, X. & Zhang, X. Recent progress in synthesis of two-dimensional hexagonal boron nitride. *J. Semicond.* **38**, 031003 (2017).
151. Laleyan, D. A. et al. Effect of growth temperature on the structural and optical properties of few-layer hexagonal boron nitride by molecular beam epitaxy. *Opt. Express* **26**, 23031–23039 (2018).
152. Chubarov, M. et al. Epitaxial CVD growth of sp^2-hybridized boron nitride using aluminum nitride as buffer layer. *Phys. Status Solidi Rapid Res. Lett.* **5**, 397–399 (2011).
153. Henry, A., Chubarov, M., Czigany, Z., Garbrecht, M. & Hogberg, H. Early stages of growth and crystal structure evolution of boron nitride thin films. *Jpn. J. Appl. Phys.* **55**, 05FD06 (2016).
154. Dahal, R. et al. Epitaxially grown semiconducting hexagonal boron nitride as a deep ultraviolet photonic material. *Appl. Phys. Lett.* **98**, 211110 (2011).
155. Lee, J. S. et al. Wafer-scale single-crystal hexagonal boron nitride film via self-collimated grain formation. *Science* **362**, 817–821 (2018).
156. Tan, L. et al. Self-aligned single-crystalline hexagonal boron nitride arrays: toward higher integrated electronic devices. *Adv. Electron. Mater.* **1**, 1500223 (2015).
157. Kobayashi, Y., Kumakura, K., Akasaka, T. & Makimoto, T. Layered boron nitride as a release layer for mechanical transfer of GaN-based devices. *Nature* **484**, 223–227 (2012).
158. Makimoto, T., Kumakura, K., Kobayashi, Y., Akasaka, T. & Yamamoto, H. A vertical InGaN/GaN light-emitting diode fabricated on a flexible substrate by a mechanical transfer method using BN. *Appl. Phys. Express* **5**, 072102 (2012).
159. Ayari, T. et al. Heterogeneous integration of thin-film InGaN-based solar cells on foreign substrates with enhanced performance. *ACS Photonics* **5**, 3003–3008 (2018).
160. Hu, S. et al. Proton transport through one-atom-thick crystals. *Nature* **516**, 227–230 (2014).
161. Schue, L., Stenger, I., Fossard, F., Loiseau, A. & Barjon, J. Characterization methods dedicated to nanometer-thick hBN layers. *2D Mater.* **4**, 015028 (2017).
162. Wang, L. et al. One-dimensional electrical contact to a two-dimensional material. *Science* **342**, 614–617 (2013).
163. Castellanos-Gomez, A. Why all the fuss about 2D semiconductors? *Nat. Photonics* **10**, 202–204 (2016).
164. Taychatanapat, T., Watanabe, K., Taniguchi, T. & Jarillo-Herrero, P. Electrically tunable transverse magnetic focusing in graphene. *Nat. Phys.* **9**, 225–229 (2013).
165. Yankowitz, M., Xue, J. & LeRoy, B. J. Graphene on hexagonal boron nitride. *J. Phys. Condens. Matter* **26**, 303201 (2014).
166. Yankowitz, M., Ma, Q., Jarillo-Herrero, P. & LeRoy, B. J. van der Waals heterostructures combining graphene and hexagonal boron nitride. *Nat. Rev. Phys.* **1**, 112–125 (2019).
167. Decker, R. et al. Local electronic properties of graphene on a BN substrate via scanning tunneling microscopy. *Nano Lett.* **11**, 2291–2295 (2011).
168. Xue, J. M. et al. Scanning tunneling microscopy and spectroscopy of ultra-flat graphene on hexagonal boron nitride. *Nat. Mater.* **10**, 282–285 (2011).
169. Yankowitz, M. et al. Emergence of superlattice Dirac points in graphene on hexagonal boron nitride. *Nat. Phys.* **8**, 382–386 (2012).
170. Tang, S. et al. Precisely aligned graphene grown on hexagonal boron nitride by catalyst free chemical vapor deposition. *Sci. Rep.* **3**, 2666 (2013).
171. Li, G., Luican, A. & Andrei, E. Y. Scanning tunneling spectroscopy of graphene on graphite. *Phys. Rev. Lett.* **102**, 176804 (2009).
172. Shi, Z. et al. Gate-dependent pseudospin mixing in graphene/boron nitride moiré superlattices. *Nat. Photonics* **10**, 743–747 (2014).
173. Tomadin, A., Guinea, F. & Polini, M. Generation and morphing of plasmons in graphene superlattices. *Phys. Rev. B* **90**, 161406(R) (2014).
174. Xian, L., Kennes, D. M., Tancogne-Dejean, N., Altarelli, M. & Rubio, A. Multi-flat bands and strong correlations in twisted bilayer boron nitride. Preprint at *arXiv* https://arxiv.org/abs/1812.08097 (2018).
175. Cao, Y. et al. Unconventional superconductivity in magic-angle graphene superlattices. *Nature* **556**, 43–50 (2018).
176. Schmidt, H. et al. Tunable graphene system with two decoupled monolayers. *Appl. Phys. Lett.* **93**, 172108 (2008).
177. Sanchez-Yamagishi, J. et al. Quantum Hall effect, screening, and layer-polarized insulating states in twisted bilayer graphene. *Phys. Rev. Lett.* **108**, 076601 (2012).
178. Luican, A. et al. Observation of Van Hove singularities in twisted graphene layers. *Nat. Phys.* **6**, 109–113 (2010).
179. Lee, D. S. et al. Quantum Hall effect in twisted bilayer graphene. *Phys. Rev. Lett.* **107**, 216602 (2011).
180. Sanchez-Yamagishi, J. et al. Helical edge states and fractional quantum Hall effect in a graphene electron-hole bilayer. *Nat. Nanotechnol.* **12**, 118–122 (2017).
181. Liu, K. et al. Evolution of interlayer coupling in twisted molybdenum disulfide bilayers. *Nat. Commun.* **5**, 4966 (2014).
182. Barbier, M., Vasilopoulos, P. & Peeters, F. M. Extra Dirac points in the energy spectrum for superlattices on single-layer graphene. *Phys. Rev. B* **81**, 075438 (2010).
183. Woods, C. R. et al. Commensurate–incommensurate transition in graphene on hexagonal boron nitride. *Nat. Phys.* **10**, 451–456 (2014).
184. Hunt, B. et al. Massive Dirac fermions and Hofstadter butterfly in a van der Waals heterostructure. *Science* **340**, 1427–1430 (2013).
185. Yeh, P.-C. et al. Direct measurement of the tunable electronic structure of bilayer MoS_2 by interlayer twist. *Nano Lett.* **16**, 953–959 (2016).
186. Chari, T., Ribeiro-Palau, R., Dean, C. R. & Shepard, K. Resistivity of rotated graphite-graphene contacts. *Nano Lett.* **16**, 4477–4482 (2016).
187. Ribeiro-Palau, R. et al. Twistable electronics with dynamically rotatable heterostructures. *Science* **361**, 690–693 (2018).
188. Senellart, P., Solomon, G. & White, A. High-performance semiconductor quantum-dot single-photon sources. *Nat. Nanotechnol.* **12**, 1026–1039 (2017).

Acknowledgements

J.D.C. acknowledges the support of Vanderbilt University for its financial support of his effort in this work. Additionally, J.D.C. and D.N.B. offer their sincere thanks to Misha Fogler for his code, used to calculate the hyperbolic dispersion of hBN in Fig. 2. J.D.C. expresses his thanks to Joseph Matson for his efforts in improving the hyperbolic polariton image in Fig. 1 and for Fig. 2b. J.H.E. appreciates support for crystal growth from the National Science Foundation, award number CMMI 1538127. This work was financially supported by the network GaNeX (ANR-11-LABX-0014). GaNeX belongs to the publicly funded 'Investissements d'Avenir' programme managed by the French ANR agency. I.A. gratefully acknowledges financial support from the Australian Research Council (via DP180100077), the Asian Office of Aerospace Research and Development grant FA2386-17-1-4064 and the Office of Naval Research Global under grant number N62909-18-1-2025. The work at Columbia University on van der Waals materials and heterostructures is supported as part of Programmable Quantum Materials, an Energy Frontier Research Center funded by the U.S. Department of Energy (DOE), Office of Science, Basic Energy Sciences (BES), under award DE-SC0019443. Research on photonic circuits is supported by AFOSR: FA9550-15-1-0478. Research on hybrid polaritonic structures is supported by ONR-N000014-18-1-2722. Development of nano-optics instrumentation at Columbia is supported by DOE-BES DE-SC0018218. D.N.B. is a Gordon and Betty Moore Foundation investigator under EPiQS Initiative Grant GBMF4533.

Author contributions

The authors contributed equally to all aspects of the article.

Competing interests

The authors declare no competing interests.

Publisher's note